Septin Filament Compaction Into Rings Requires the Anillin Mid2 and Contractile Ring Constriction

Federica Arbizzani, Manos Mavrakis, Marta Hoya, Juan Carlos Ribas, Sophie Brasselet, Anne Paoletti, Sergio Rincon

Septin filament compaction into rings requires the anillin Mid2 and contractile ring constriction

Federica Arbizzani[1], Manos Mavrakis[2], Sophie Brasselet[2], Anne Paoletti[1]* and Sergio A. Rincon[3]*

Running title: Mid2 promotes fission yeast septin ring assembly

[1] Institut Curie, PSL University, CNRS UMR 144, F-75005, Paris, France.

[2] Aix Marseille Université, CNRS, Centrale Marseille, Institut Fresnel, UMR 7249, Marseille, France.

[2] Instituto de Biología Funcional y Genómica and Departamento de Microbiología y Genética, Consejo Superior de Investigaciones Científicas (CSIC) / Universidad de Salamanca, Salamanca, 37007 Spain.

*corresponding authors and equal contribution

Correspondance: anne.paoletti@curie.fr and sarpadilla@usal.es

SUMMARY

Septin filaments assemble into high-order molecular structures that associate with membranes, acting as diffusion barriers and scaffold proteins crucial for many cellular processes. However, how septin filaments organize in such structures is still not well understood. In this study, we used fission yeast to explore septin filament organization during cell division and decipher key factors responsible for their regulation. Live-imaging and polarization microscopy analysis uncovered that septin filaments are initially recruited as a diffuse meshwork surrounding the acto-myosin contractile ring (CR) in anaphase, which undergoes compaction into two rings when CR constriction is initiated. We found evidence that the anillin-like protein Mid2 is necessary to promote this novel compaction step, possibly acting as a bundler for septin filaments. We also found that Mid2-driven septin compaction requires inputs from the Septation Initiation Network (SIN) as well as CR constriction or the β-1-3 glucan synthase Bgs1. This work highlights the complex regulations that allow the coordination between septin ring assembly and cell cycle progression.

INTRODUCTION

Cytokinesis is an irreversible process which must precisely partition an equal set of the replicated chromosomes and organelles into each daughter cell. Defects in this process can lead to chromosome mis-segregation or aneuploidy, a hallmark of cancer ((Storchova and Pellman, 2004) (Fujiwara et al., 2005) (Lacroix and Maddox, 2012)). Cytokinesis completion requires the participation of different components of the cytoskeleton, namely, the actin cytoskeleton at the basis of the contractile ring (CR) that pinches in the plasma membrane to create the cleavage furrow, microtubules involved in division plane signaling in animal cells, as well as septins which are present at the division site from yeast to mammals.

Septins are unique cytoskeletal components capable of self-assembling to form high-order molecular structures of varied shapes such as filaments and rings. Their ability to interact with cellular membranes through interaction with negatively charged phospholipids, such as phosphatidylinositol 4,5-bisphosphate (PIP2) as well as actin filaments and microtubules allows them to participate in many biological processes, working as diffusion barriers for protein compartmentalization and/or scaffolds for protein-protein interactions ((Bertin et al., 2010) (Saarikangas and Barral, 2011) (Mostowy and Cossart, 2012) (Bridges et al., 2014) (Bridges and Gladfelter, 2015) (Bridges et al., 2016) (Marquardt et al., 2019). These conserved GTP-binding proteins were initially discovered in budding yeast, based on their role in cytokinesis, a function which was found to be conserved in animals ((Hartwell, 1971) (Neufeld and Rubin, 1994) (Gladfelter et al., 2001) (Surka et al., 2002) (Kozubowski et al., 2005) (Versele and Thorner, 2005) (McMurray and Thorner, 2009) (El Amine et al., 2013) (Founounou et al., 2013) (Cauvin and Echard, 2015)). Importantly, septins in budding yeast serve as a scaffold for the sequential and ordered assembly of the acto-myosin based CR ((Juanes and Piatti, 2016) (Meitinger and Palani, 2016) (Bhavsar-Jog and Bi, 2017)). Later on, when CR constriction occurs, septins act as cortical barriers to create specialized confined zones at the cleavage furrow where membrane reorganization and septum formation happen before cell division ((Dobbelaere and Barral, 2004)).

In budding yeast septin organization undergoes multiple transitions during the cell cycle. In early G1, septins initially assemble as a patch-like structure at the presumptive

bud site. Upon bud emergence, this patch narrows to form a single ring marking the future site of bud growth. Once the bud has formed, the septin ring extends into an hourglass-shaped collar present at the bud neck until mitotic entry. At cytokinesis onset, the septin hourglass splits into two distinct rings that sandwich the CR ((Gladfelter et al., 2001)). Finally, after cell division, the septin rings disassemble and the septin subunits are recycled for a new cycle to begin ((McMurray and Thorner, 2009)).

One important factor in the organization of septins is the conserved protein anillin, whose disruption leads to defects in animal cytokinesis ((Oegema et al., 2000) (Somma et al., 2002) (Echard et al., 2004) (Field et al., 2005) (Straight et al., 2005) (Zhao and Fang, 2005) (Hickson and O'Farrell, 2008) (Piekny and Glotzer, 2008). Indeed, anillin bridges septins and the CR during cell division ((Oegema et al., 2000) (Kinoshita et al., 2002) (Field et al., 2005) (Kechad et al., 2012) (Liu et al., 2012)). *In vitro* studies have shown that anillin can bind septin and actin filaments. Animal anillin interacts with septins and PIP2 through a C-terminal PH domain located after the anillin homology domain ((Piekny and Glotzer, 2008) (Piekny and Maddox, 2010) (Kechad et al., 2012) (Liu et al., 2012)). The C-terminal region of Bud4, the anillin-like protein in budding yeast, is important to direct septin organization during bud site selection and bud growth and to preserve the integrity of the septin ring during cytokinesis ((Kang et al., 2013) (Wu et al., 2015)).Thus, in *bud4Δ* mutants the septin double ring disassembles during cytokinesis (Kang et al., 2013)), whereas the overexpression of Bud4 leads to the formation of extra septin structures. More recently, polarized fluorescence microscopy studies have described a key role of Bud4 in the reorientation of septin filaments in the hourglass to double ring transition ((McQuilken et al., 2017)).

The fission yeast *Schizosaccharomyces pombe*, a recognized model system for cytokinesis studies, is a rod-shaped organism that divides by the assembly and constriction of a medially placed actomyosin-based CR. *S. pombe* has two anillin-like proteins, Mid1 and Mid2, with non-overlapping functions (Berlin et al., 2003b) (Tasto et al., 2003). Mid1 accumulates at the medial cortex at mitosis onset, where it recruits components involved in CR assembly ((Pollard and Wu, 2010) (Lee et al., 2012) (Rincon and Paoletti, 2012) (Rincon and Paoletti, 2016)). CR constriction and synthesis of the

extracellular cell wall separating the two daughter cells is triggered upon mitotic exit by the SIN pathway, related to the budding yeast Mitotic Exit Network (MEN) and the metazoan Hippo pathway ((Hergovich et al., 2006)). *S. pombe* septins were identified by sequence homology with the *S. cerevisiae* counterparts ((Wood et al., 2002)). Spn1-4 are expressed in vegetatively growing cells and localize to the division site. However, differently from *S. cerevisiae*, where septins are necessary for CR formation, fission yeast septins are recruited after the CR has fully assembled. Septins form first a single ring in late mitosis which splits in two during CR constriction and septum formation. This double ring does not constrict together with the CR, but remains on the cell surface to delineate the boundaries of the cleavage furrow and dissociates after cell separation ((Berlin et al., 2003b) (Tasto et al., 2003) (Wu et al., 2003) (An et al., 2004) (Juanes and Piatti, 2016)). Septin mutants have defects in cell-cell separation since septins have a key role, in concert with the exocyst complex, in the delivery of the two septum hydrolytic enzymes (Agn1 and Eng1) to the area around the septum, regulating thereby the step that finishes cytokinesis (Martin-Cuadrado et al., 2005)). Recently, it has also been shown that septins play a role in driving the proper recruitment and maintenance in the septum region of the SIN effector kinase Sid2 and of the glucan synthase enzymes Bgs1 and Ags1, to guarantee a successful cytokinesis ((Zheng et al., 2018)). Mid2 localizes at the division site in a septin-dependent manner ((Berlin et al., 2003b)). FRAP analysis has revealed that, in the absence of Mid2, septins are more dynamic, indicating a role of Mid2 in septin organization ((Berlin et al., 2003b)). Overexpression of a non-degradable Mid2 mutant let septin filaments persist through the next cell cycle, indicating that Mid2 is also involved in septin ring maintenance ((Tasto et al., 2003) (An et al., 2004)).

How septins and Mid2 are precisely regulated in space and time to properly perform their function and how Mid2 contributes to septin ring organization remains elusive. Here, by using live cell imaging and precise timers for mitotic progression we describe in detail septin and Mid2 behavior in fission yeast. Our approach identified a new step in septin ring assembly: septin filament compaction from a loose meshwork surrounding the CR into a tight ring when CR constriction is initiated. We show that this step requires Mid2, which has the properties of a bundler for septin filaments

promoting their compaction. Polarization microscopy in living dividing cells show that septin filaments transition from a disorganized state to a highly ordered state where they become parallel to the CR actin filaments during CR constriction, in a mechanism dependent on Mid2. Finally, we show that the process of septin compaction requires the SIN pathway signaling and CR constriction. In summary, we show that septin filaments organization depends on the anillin-like protein Mid2 and on signaling inputs that coordinate cytokinesis events in fission yeast.

RESULTS

Septins form a diffuse network in the vicinity of the CR before compacting into a ring structure

Fission yeast septins localize to the division site where they form non-contractile rings defining the edge of the cleavage furrow while the CR constricts and the septum is built (Berlin et al., 2003a, Tasto et al., 2003). However, relatively little is known about how septin rings assemble. We therefore decided to characterize by time-lapse imaging the dynamic organization of septins with respect to spindle assembly and elongation, used as a proxy for mitosis progression, and CR assembly and constriction.

To do so, we created a strain expressing the septin Spn1 C-terminally fused to GFP, as well as the regulatory light chain of myosin II Rlc1 fused to mCherry to monitor the CR, and the spindle pole body (SPB) component Sid4 tagged with mCherry to monitor the mitotic spindle. Indeed, since septins function strictly as heteromeric complexes, imaging Spn1 is sufficient to have an overview of the whole septin network (An et al., 2004). In these movies, SPB separation was defined as a timer for mitotic entry (t=0 in Fig 1).

Septins appeared on the cortex as a band surrounding the CR about 18 minutes after SPB separation, when the SPBs were the furthest apart, corresponding to maximum spindle elongation in anaphase (Fig 1A and 1D, t=18.6 ± 2.3 min). 7 minutes later, septins compacted into a tight ring structure (t=25.6 ± 2.8 min), concomitant with the initiation of CR constriction (t=26.1 ± 2.9 min). This compaction phenomenon is best visualized on enlargements of the medial region of the cell recorded at 1-minute intervals (Fig 1C left, dark green asterisk). About 20 minutes later, by the end of CR constriction (t=48.5 ± 3.6

min), septins were visualized as a double ring (t=43.4 ± 6.5 min, red asterisk). Eventually, septins re-spread to the new cell tip generated when the two sister-cells separated from one-another by cleavage of the septum (yellow asterisk).

Quantitative analysis of the septin signal further revealed that septin intensity raised for a period of about 15 minutes after they appeared on the medial cortex. The intensity then stayed roughly constant for 30 minutes before decreasing rapidly over 10 minutes (Fig 1F). Furthermore, analyzing the width of the cortical region on which septins were distributed revealed a two-fold reduction in width, from 1.4 ± 0.1 µm at their appearance to 0.75 ± 0.1 µm after compaction (n=30, Fig 1G light green dots).

To conclude, this detailed live analysis of septins establishes the timing of the major transitions in septin organization and reveals a new step in the process of septin ring assembly that we have named compaction.

The anillin Mid2 is necessary for septin ring compaction

A similar imaging strategy was taken to define the dynamic organization of the anillin-like protein Mid2, known to co-localize with septins and modulate their dynamics ((Berlin et al., 2003b) (Tasto et al., 2003)). Using a strain expressing Mid2 C-terminally fused to the green fluorescent protein ENVY, as well as Rlc1-Cherry and Sid4-mCherry, we found that Mid2 appeared 8 minutes later than septins (t=26.9 ± 2.5 min), coincident with the time of septin compaction (Fig 1C right, light green asterisk in the Mid2 kymograph and Fig 1C left, dark green asterisk in the Spn1 kymograph, Fig 1D-E) and CR constriction (t=25.2 ± 2.4 min, Fig 1B-E). Later on, Mid2 compacted slightly (Fig 1C right, dark green asterisk), appeared as two rings concomitantly to the double septin rings (Fig 1C, red asterisk) and spread out on the newly formed cell tips upon daughter cell separation (Fig 1C right, yellow asterisk).

Quantitative analysis of Mid2 signal confirmed the late recruitment of Mid2 compared to septins and showed that its intensity raised for about 30 minutes, stayed constant for 10 minutes and decreased rapidly, similarly to septins (Fig 1F). Moreover, we found that Mid2 was recruited to a narrower region than septins and its compaction was limited compared to septins with the width of the Mid2 domain decreasing from 1.1 ± 0.1 µm at appearance to 0.8 ± 0.1 µm after compaction (Fig 1G dark green dots).

The coincidence between CR constriction, septin compaction and Mid2 recruitment suggested that these events may be coupled. To determine if this was the case, we first tested whether Mid2 was involved in septin compaction. To do so, we analyzed septin ring assembly in a *mid2* deletion mutant ((Berlin et al., 2003b)), using the same markers for mitosis and cytokinesis progression as before. Time-lapse movies showed that in *mid2Δ* cells, initial septin recruitment occurred normally (Fig 2A-E), but septin intensity stopped increasing prematurely, about 8 minutes after septins appeared, i.e. at the time when Mid2 normally appears (Fig 2F). As a consequence, septin maximum intensity was decreased by 3-fold in *mid2Δ* cells compared to control cells (n=6 for both samples) (Fig 2F). Furthermore, septin compaction was completely abolished (Fig 2C, 2G). Instead, septins retained a diffuse distribution around the CR (Fig 2C and S1A). As a consequence, splitting into two rings did not occur. Finally, whereas the CR constriction took place normally (Fig 2-E and S1B), cell separation was delayed and septin rings persisted during the next cell cycle, as reported in a *mid2* deletion mutant (Fig 2A-E; (Berlin et al., 2003a, Tasto et al., 2003)).

Mid2 may function as bundler for septin filaments

The fact that Mid2 is necessary for septin compaction, suggested that Mid2 may function as a bundler for septin filaments promoting their alignment and assembly into a ring structure. To perform this activity, Mid2 should be able not only to interact with septins, but also to dimerize or multimerize in order to bridge together two or more septin filaments.

In line with this hypothesis, Mid2 co-immunoprecipitated with septins (see Fig S3C). To test if Mid2 self-associates, we designed co-immunoprecipitation assays between differentially tagged versions of Mid2 co-expressed in the same cells. These experiments were performed in the presence or in the absence of Spn1 to exclude the detection of differentially tagged molecules of Mid2 bridged by septin filaments. Our experiments show that Mid2-mEGFP co-immunoprecipitates with Mid2-13Myc regardless of the presence of septin filaments (Fig 3A and B).

In order to map the Mid2-Mid2 interaction site, we also performed immunoprecipitations with a truncated version of Mid2 lacking the PH domain (Mid2 ΔPH) or with the isolated PH domain (see Fig 3C for Mid2 domains organization).

Interestingly, Mid2-ΔPH-mEGFP co-immunoprecipitated with Mid2-13Myc and Mid2 PH domain also showed the ability to self-interact in co-immunoprecipitation assays, even in the absence of septin filaments (Fig 3A and B). This altogether indicates that Mid2 has the ability to form structures of higher molecular order and that both the PH domain and the N-terminal part of the molecule may play a role in this process. Since Mid2 arrival at the cortex also coincides with septin compaction and Mid2 is necessary for this step, our biochemical data support the hypothesis that Mid2 may promote compaction by bundling septin filaments.

Septins and Mid2 form wide bands surrounding the CR when cells are blocked in mitosis

Our work shows that septin filaments appear at a very precise time in mitosis, when the anaphase spindle length is maximum, and compact into rings when Mid2 appears and the CR starts constricting. This provides evidence for a tight coupling between septin ring assembly and cell cycle progression. To get insight into how this coupling is achieved, we first analyzed the localization of Spn1 and Mid2 in mutants blocked in mitosis, with a high cyclin-dependent kinase (CDK) activity. We first used the cold sensitive β-tubulin mutant *nda3-KM311* expressing Spn1-GFP or Mid2-ENVY together with Rlc1-mCherry and Sid4-mCherry. Upon cold treatment, cells were blocked in mitosis carrying a CR, and formed a large band of septins or Mid2 surrounding the CR instead of the septin or Mid2 ring detected in control cells (Fig 4A left). Interestingly, Spn1-GFP and Rlc1-mCherry intensity measurements by linescans along the cell axis showed a decrease in Spn1-GFP signal at the exact position of the CR (Fig 4A right and Fig S2B and C). Furthermore, imaging these cells at 1-hour intervals after the temperature shift showed that the width of the septin domain gradually increased in *nda3-KM311* cells (from 1.2 µm ± 0.03 after 1 hour at 18°C to 2.4 µm ± 0.2 after 7 hours at 18°C), while narrow rings were always present in control cells (0.9 µm ± 0.03, Fig S2A). A similar situation was observed for the Mid2 domain, its width increasing from 1.0 µm ± 0.1 after 1 hour at 18°C to 2.0 µm ± 0.1 after 7 hours in *nda3-KM311* cells compared to narrow rings in control cells (0.9 µm ± 0.4, Fig S2A). Release from the mitotic block by transferring the cells back to 25°C for 1 hour resulted in a compaction of both septin and

Mid2 domains with the domain widths decreasing to 1.2 µm ± 0.1 and 1.3 µm ± 0.2, respectively (Fig S2A).

We also used the thermo-sensitive kinesin-5 *cut7-24* mutant, which forms a monopolar mitotic spindle at 36°C, producing a temporary cell cycle arrest in metaphase with a high CDK activity (Fu et al., 2009, Hagan and Yanagida, 1990, Hagan and Yanagida, 1992). Live cell imaging of the Spn1-GFP Rlc1-mCherry Sid4-mCherry strain in the wild type cells at 36°C slightly accelerated mitosis progression compared to 25°C (Fig 4B and C compared to Fig 1A and D), but septin appearance occurred again at the time of maximum spindle elongation and septin compaction coincided with the initiation of CR constriction, like at 25°C. In the *cut7-24* mutant, since no SPB separation could be observed, the time of transfer to 36°C was defined as time 0 for this experiment. The timing measured in this background can therefore not be compared to those measured in the wild type background. In the *cut7-24* mutant, septins appeared 9 minutes after the temperature shift in a large band (1.7 ± 0.2 µm compared to 1.45 ± 0.1 µm in control cells, Fig 4F) and were excluded from the CR as seen in *nda3-KM311* cells. Unlike in control cells, where septins compacted to 0.9 ± 0.05 µm, these bands became slightly larger over time in *cut7-24* cells (2.0 ± 0.1 µm Fig 4D-F), until they escaped the cell cycle arrest 29.6 ± 4.4 min in mean after transfer to 36°C, as visualized by the initiation of CR constriction, which was again coincident with septin band compaction (t=29.3 ± 4.4 min). Later on, septins were observed as two rings at t=41.9 ± 7.3 min and re-spread along the cell cortex at t=55.6 ± 5.1 min (Fig 4D and E).

Live cell imaging of the Mid2-ENVY Rlc1-mCherry Sid4-mCherry *cut7-24* mutant strain at 36°C showed that Mid2-ENVY formed a faint band surrounding the CR that enlarged slightly over time (Fig S4C and E), until cells escaped mitosis and CR constriction initiated (t=33.6 ± 2.3), coincident with Mid2 compaction (t=33.4 ± 2.5, Fig S4C-E). Ring splitting and re-spreading were strongly delayed (t=45.7 ± 1.2 and t=66.4 ± 5.2, respectively) (Fig S4D).

Overall, these data suggest that high CDK activity does not interfere with initial septin and Mid2 recruitment. However, later events, such as further septin accumulation at the division site and septin compaction and re-spreading may require a reduction in CDK

activity. This in turn suggests that Mid2 bundling activity may be impaired in these conditions.

This prompted us to investigate if Mid2 had still the ability to self-interact in this context. To do so, we performed co-immunoprecipitations between Mid2-13Myc and Mid2-GFP, Mid2 ΔPH-GFP or the single PH domain of Mid2 tagged with GFP in the control or *nda3-KM311* mutant cells, after 8 hours of incubation at 18°C to block cells into mitosis (Fig S3A). These experiments did not reveal any modification in the ability of Mid2 to self-interact.

We then tested if high CDK activity could reduce the avidity of Mid2 for septins. To test this hypothesis, co-immunoprecipitation assays between Spn1-GFP and Mid2-13Myc were performed in control and *nda3-KM311* cells after 8 hours of incubation at 18°C or after 8 hours at 18°C followed by 1 hour at 25°C to release cells from the mitotic block (Fig S3B). Again, these experiments did not reveal significant differences in the ability of Mid2 to interact with septins.

Altogether, these data suggest that, although Mid2 is necessary for septin compaction, it is not proficient for this function when CDK activity is high, independently of its ability to self-interact or to interact with septins. Since Mid2 is hyperphosphorylated during mitosis (Tasto et al., 2003), one hypothesis is that Mid2 phosphorylation prevents septin compaction. Or else, CDK activity regulates septin compaction independently of Mid2.

Mid2 controls the orientation of septin filaments

In order to test further our hypothesis that Mid2 functions as a septin filament bundler and to get insights into the role of Mid2 in septin filament organization, we decided to measure septin filament organization using polarization-resolved fluorescence microscopy ((Vrabioiu and Mitchison, 2006) (DeMay et al., 2011b) (DeMay et al., 2011a) (Kress et al., 2013) (Wang et al., 2013)). Polarimetry measurements with the regular Spn1-GFP fusion, which includes a flexible linker between the septin and the GFP, revealed randomly oriented GFP dipoles at all stages of cytokinesis, consistent with the flexibly-linked GFP exploring orientations in all directions relative to Spn1 (Fig S5A).

Thus, to use dipole orientation measurements of the GFP as a readout of septin filament orientation, the mobility of GFP relative to Spn1 had to be minimized. We therefore screened for Spn1-GFP fusions in which several aminoacids between the C-terminus of Spn1 and the N-terminus of GFP were deleted without impairing Spn1 localization and function nor GFP fluorescence, and identified a fusion of Spn1 to rotationally constrain GFP (conGFP), Spn1-conGFP (see methods for details).

The Spn1-conGFP construct was produced from the genomic *locus*, under the control of the promoter of *spn1*, in a strain expressing Rlc1-mCherry Sid4-mCherry. This strain had a wild type phenotype indicating that the fusion was fully functional. Accordingly, Spn1-conGFP localized and redistributed similarly to Spn1-GFP (Fig S5B and C).

We measured GFP dipole orientation at four different stages during cytokinesis, namely septin recruitment (Appearance), septin compaction (Early), CR constriction (Late), and CR disassembly (Post-constriction) in this strain. We found that GFP dipoles were highly disordered when septins are first recruited to the division site, as evidenced by the random distribution of angles between the GFP dipoles and the axis of the CR (Fig 5A). However, at later stages when septins compact into tight rings and throughout CR constriction, the distribution of angles between GFP dipoles and the CR axis became narrow, with GFP dipoles mostly oriented perpendicular to the CR axis (Fig 5A). Their distribution eventually started becoming broader again after CR disassembly, when the septin rings start to collapse. The narrowing of the GFP dipole orientation distributions upon and throughout CR constriction, which also seems to persist post-constriction, indicates that the associated septin filaments are highly organized during these stages.

To determine the orientation of the GFP dipoles relative to septin filaments and be able to deduce septin filament orientation with respect to the CR axis, we took advantage of a Spn4-GFP fusion, (Fig S5D and E; see methods for detains), which, in addition to its normal localization to the septin ring (white asterisks in Fig S5D and E), also assembled into ectopic elongated cytoplasmic bars (arrows in Fig S5D). These ectopic bars most likely represent bundles of tightly packed parallel septin filaments, similar to elongated bar-like septin structures induced in *Ashbya gossypii* upon treatment with the septin

filament stabilizing drug forchlorfenuron (DeMay et al., 2011a) and very similar to the ectopic bar-like structures detected in *spn2*Δ cells containing both Spn1 and Spn4 (An et al., 2004). GFP dipoles were perpendicular to these septin bars (Fig S5D) suggesting that the septin filaments are oriented perpendicular to the GFP dipole in the Spn4-conGFP fusion. Importantly, GFP dipoles were also perpendicular to the CR axis during CR constriction and disassembly in these cells (Fig S5E), suggesting that septin filaments run parallel to the CR axis. Given that Spn4 is in a complex with Spn1 (An et al., 2004) we deduce that the septin filaments in the Spn1-conGFP construct are also oriented perpendicular to the GFP dipoles, and propose that initially randomly organized septin filaments orient parallel to the CR upon compaction and keep this orientation throughout CR constriction, progressively losing their organization after CR constriction as septin rings progressively collapse (Fig 5D)..

Septin filament orientation was then analyzed in *mid2Δ* cells. Similar to the wild type, septin filaments appeared in a very disorganized manner in *mid2Δ* cells (Fig 5B). However, as CR constriction took place, GFP dipoles failed to reorient perpendicular to the CR (Fig 5B). Septin filaments also failed to align in *nda3-KM311* cells where CDK activity is high (Fig 5C).

Overall, this data indicates that Mid2 contributes to the orientation of septin filaments parallel to the CR axis, supporting the hypothesis that Mid2 functions as a septin bundler (Fig 5D) during the septin compaction phase. Moreover, Mid2 bundling activity is negatively regulated by CDK activity in a direct or indirect manner, preventing septin orientation and compaction in early mitosis.

SIN activity and CR constriction are required for normal septin accumulation and compaction at the division site

Since septin compaction is coincident with CR constriction, an event known to be triggered by the SIN pathway (McCollum and Gould, 2001), we next wondered if septins and Mid2 were also under the control of this pathway.

To test this hypothesis, we analyzed the behavior of septins in the temperature sensitive hypo-active SIN mutant *sid2-250* at the non-permissive temperature of 36°C (Balasubramanian et al., 1998, Sparks et al., 1999). Live cell imaging of *sid2-250* cells expressing Spn1-GFP Rlc1-mCherry Sid4-mCherry revealed that in the majority of cells septins appeared as a diffuse cortical band at the normal timing compared to control cells (Fig 6A-D). However, the intensity of the septin signal was diminished by ~ 4.5-fold (Fig 6E) and compaction failed in 75% cells, while a loose compaction was observed in the remaining 25%. Indeed, quantification of the extent of compaction showed that, while in control cells the width of the septin domain decreased from 1.5 ± 0.1 µm to 0.9 ± 0.1 µm between appearance and compaction state, in the majority of *sid2-250* mutant cells, the initial width of the septin domain increased instead from 1.6 ± 0.1 µm to 1.9 ± 0.1 µm in a similar period of time, although it decreased in a minority of cells (from 1.6 ± 0.1 µm to 1 ± 0.1 µm (Fig 6F).

The lack of septin compaction suggested a possible defect in the function of Mid2. Therefore, the behavior of Mid2 was analyzed in *sid2-250* cells expressing Mid2-ENVY Rlc1-mCherry Sid4-mCherry (Fig S6A-D). These cells displayed a strong defect (3.5 fold) in the accumulation of Mid2 (Fig S6E), similar to the one observed in Spn1 accumulation. Moreover, Mid2-ENVY did not compact at all, as seen in 75% cells for Spn1-GFP.

Altogether, these data suggest that the SIN pathway is not responsible for the initial recruitment of septins or Mid2, but is required for their accumulation. The defects observed in septin and Mid2 compaction also suggest that the SIN may be required for this event.

Since the SIN pathway triggers CR constriction ((Liu et al., 2000) (Jin et al., 2006)), we next wondered if the SIN acts directly on septin compaction or indirectly by inducing CR constriction.

To test this, we decided to use the β-glucan synthase mutant *cps1-191* which halts cytokinesis progression with an assembled CR that cannot constrict. Interestingly, it had been shown that the SIN is active in this mutant and required for the stability of the CR ((Liu et al., 2000)), which provides the best scenario to answer our question. Spn1-GFP and Mid2-ENVY behavior were analyzed in a *cps1-191* mutant expressing Rlc1-mCherry

and Sid4-mCherry at restrictive temperature (Fig 7A-D and S7A-D). Both proteins showed a very defective accumulation (Fig 7E and S7E), septins did not compact (Fig 7F) and eventually dissociated from the division site, even when the CR remained stable (Fig 7C and D and Fig S7C and D).

Altogether, these data strongly suggest that the SIN pathway acts on septins and Mid2 accumulation and compaction, by inducing CR constriction.

Overall, our results indicate that the anillin-like protein Mid2 promotes septin accumulation at the division site and controls septin filament alignment to assemble the septin rings in a process strictly regulated by the cell cycle progression and CR constriction.

DISCUSSION

The assembly of macromolecular structures is a distinctive feature of cytoskeletal elements. Septins are GTP-binding proteins with the ability to form non-polar filaments, which can assemble into a variety of membrane-associated structures in cells such as filament networks or rings (Ong et al., 2014). A number of factors influence the ability of septins to get assembled into those structures, such as the septin monomers themselves, the lipid bilayer composition, post-translational modifications or regulatory proteins.

Here, we investigated the role of the septin-binding protein, Mid2 in the assembly of supramolecular septin filament structures, using fission yeast as a model system. Mid2 is an anillin ortholog, previously involved in the stability of the septin ring assembled during cytokinesis ((Berlin et al., 2003b) (Tasto et al., 2003)). Similar to other anillin orthologs, such as *Saccharomyces cerevisiae* Bud4, Mid2 is only recruited at the end of cytokinesis. In contrast to budding yeast, in which septins are first recruited to the presumptive bud site at the onset of G1 (reviewed in (Juanes and Piatti, 2016)), in fission yeast septins only localize to the cortex during cell division. Indeed, septin recruitment requires the assembly of the CR prior to their localization.

Our data show that septins localize to the division site as a diffuse band that compacts into a tight ring by the time of CR constriction. This compaction is a novel step in the behavior of septins, coincident with the appearance of Mid2, suggesting a cause-effect relationship. Accordingly, the lack of Mid2 results in the inability of septins to compact.

How might Mid2 trigger septin band compaction? One possibility is that Mid2 serves as a bridge connecting septin filaments. In fact, anillin is a scaffolding protein, able to interact with many other proteins ((Field et al., 2005) (Piekny and Glotzer, 2008)). Anillin (and Mid2) contains a C-terminal septin-interacting domain. If Mid2 were to bundle septin filaments, it should be able to interact with itself so that each molecule could bind to a different septin filament. Our biochemical analysis of Mid2 self-association shows that Mid2 can interact with other Mid2 molecules via its C-terminal PH domain, but also through upstream regions. This suggests that at least two molecules of Mid2 could bridge two septin filaments together. Increasing levels of Mid2 would contribute to septin filaments compaction into a tight ring. Importantly, in the absence of Mid2, septin accumulation is strongly affected; since Mid2 recruitment to the division site is strongly dependent on septins ((Berlin et al., 2003b) (Tasto et al., 2003)), we propose that septins and Mid2 establish a positive feedback loop to get properly accumulated at the division site.

Septin filaments show a dynamic organization pattern during cell cycle progression. Our data based on polarization microscopy let us conclude that septin filaments are not organized when they first appear at initial stages of cytokinesis. Coincident with the arrival of Mid2, septin filaments become aligned parallel to the CR, a pattern that is lost upon deletion of *mid2*. This strongly supports the notion that Mid2 functions to bridge septin filaments and organize them. In budding yeast, after the initial recruitment to the bud site and the early stages of ring formation septins show a "fluid" state, followed by "frozen" state once the ring transforms into a collar ((Caviston et al., 2003) (Dobbelaere et al., 2003)); after ring duplication septin dynamics increases again. At the same time, during the collar stage, septin filaments are parallel to the mother-bud axis ((Vrabioiu and Mitchison, 2006)), while they reorganize to become parallel to the CR in later stages ((DeMay et al., 2011a)) in a process that might implicate disassembly and reassembly of septin filaments ((Ong et

al., 2014)). This process might be different in fission yeast, where septin filaments only transition from a disordered to an ordered organization, parallel to the CR. In any case, anillin-like proteins, seem to play the conserved role of septin filament reorganization and septin ring stabilization, as it is also the case for budding yeast anillin Bud4 ((McQuilken et al., 2017)).

What signals trigger the dynamic behavior of septins? SUMOylation, acetylation and phosphorylation are the best characterized posttranslational modifications involved in septin regulation. Our data is consistent with a tight control from the cell cycle machinery. In wild type cells, septin recruitment to the division site takes place during anaphase, when mitotic spindle reaches its maximum length. Mid2 appearance happens 8 minutes later, by the time of detectable CR constriction. Analysis of septin and Mid2 behavior in the beta-tubulin mutant *nda3-KM311* or the kinesin-5 mutant *cut7-24*, blocked at early stages of mitosis demonstrate that both strongly accumulate at the division site when CDK activity is high. Although we have no proof of a direct phosphorylation by CDK, Mid2 is highly phosphorylated during septation (Tasto et al., 2003) and our non-published data show a number of CDK consensus sites phosphorylated in *nda3-KM311* blocked cells. This would not be surprising since both septins and anillin orthologs have been shown to be direct targets of CDK in other model systems (Sinha et al., 2007) (Eluere et al., 2012).

Detailed observation of septins and Mid2 in mitotic blocked cells opens two questions.

First, septin and Mid2 initial meshworks are excluded from the precise CR position on the cortex, raising the question on the molecular mechanisms at work to allow such an exclusion and whether streric hindrance on the plasma membrane surface might be sufficient. Whatever the mechanisms, it can be inferred from this observation, that the compaction of the two septin domains on each side of the CR, might immediately produce a double septin ring, although it may not be detectable until the septum has grown enough to push them apart, allowing the observation of the septin double ring. Initial septin recruitment observation by super-resolution microscopy will contribute to clarify this point.

Second, even though septins and Mid2 co-localize and interact in this context, this is not sufficient to trigger septin ring compaction. This suggests that another mechanism contributes to septin ring compaction. It might involve posttranslational modifications of Mid2, an additional protein working together with Mid2 to promote septin filament bundling, or yet another mechanism to be identified.

Importantly, compaction of the septin filaments is coincident with the onset of the CR constriction triggered by the SIN pathway and we found the SIN plays a critical role in septin ring assembly. A possible explanation for this is the poor accumulation of Mid2 in the absence of SIN activity, which might result in the poor accumulation of septin filaments and also affect their reorganization. This suggests the SIN might target Mid2 to control septin accumulation and compaction.

However, we also found that the β (1,3) glucan synthase mutant *cps1-191*, in which CR constriction is defective but the SIN pathway is active ((Liu et al., 2000)) phenocopies the SIN mutant *sid2-250* in terms of septin defects. Although we cannot rule out the the hypothesis that the SIN may target Mid2, this demonstrates that SIN activity on its own is not sufficient to trigger the full accumulation of septins and Mid2 and the compaction of septin filaments. Rather, CR constriction by itself or the the β (1,3) glucan synthase might cooperates with Mid2 to promote septin filament accumulation and reorientation. One possibility to explore in the future is that CR constriction or the initial deposition of septum material by the β (1,3) glucan synthase may modify the plasma membrane locally, favoring Mid2 and septin accumulation on the cortex and septin filament reorientation.

In summary, we have shown that the crosslinking activity of the anillin-like protein Mid2 promotes the compaction of an initial broad band of septin filaments into tight rings at the onset of CR constriction. The activity of the SIN is necessary but not sufficient to trigger this effect and CR constriction itself, or the β (1,3) glucan synthase downstream of the SIN may be the real trigger. It will be interesting to explore whether other anillin-like proteins play similar roles in other systems

MATERIAL AND METHODS

Yeast genetics and culture

Standard *S. pombe* media and genetic manipulations were used ((Moreno et al., 1991)). All strains used in the study were isogenic to wild type 972 and are described in Supplemental Table S1. Strains from genetic crosses were selected by random spore germination and replica in plates with appropriate supplements or drugs.
Transformations were performed by using the lithium-DTT method. 20 ml of exponentially growing cells (optical density 0.5-0.8) were harvested by centrifugation and washed with 10 mM Tris HCl pH 7.4. After a second centrifugation, they were re-suspended in 100 mM lithium acetate with 10 mM DTT and were incubated on an orbital wheel at room temperature for 40 minutes. 100 µl of these cells were mixed with 80µl of 100mM lithium acetate, 10 µl of single stranded DNA from salmon testes (D9156-5ML, Sigma) and 2 µg of the desired plasmid or the purified PCR product. After 10 minutes of incubation on an orbital wheel, 300 µl of PEG 4000, previously diluted 1:1 in 100 mM lithium acetate, were added. After a second round of 10 minutes on the wheel, 15 µl of DMSO were added and the cells were subjected to heat shock at 42°C for 20 minutes in a water bath. Cells were then plated on the appropriate selection plates.

Production of mutant and tagged strains

Wild type *mid2* was fused to the green fluorescent tag ENVY ((Slubowski et al., 2015)) or to the 13Xmyc tag at its C-terminus by PCR from the plasmid pFA6a-ENVY-kanMX6 or pFA6a-13Xmyc-natMX6, respectively, as described in ((Bahler et al., 1998)).

An integration plasmid for Mid2 constructs was produced by insertion of 1 kb of the *mid2* promoter (*pmid2*) and terminator (*tmid2*) into pFA6a-mEGFP-kanMX6 ((Bahler et al., 1998)) between *SalI* and *BamHI* sites and *PmeI* and *SacII* sites, respectively. The *mid2* open reading frame (ORF) was then inserted upstream of mEGFP between *BamHI* and *XmaI*. Full length *mid2* was replaced between *BamHI* and *XmaI* sites by the single PH domain of Mid2 (582–685aa). pFA6a-GFP-kanMX6-derived plasmid was digested with *Not*I before transformation.
Constructs expressing Mid2-mEGFP full length, Mid2ΔPH-mEGFP (1-581aa) and the C-terminal PH domain of Mid2 (aa 582-685) tagged with mEGFP were integrated at the

leu1 locus under the control of their own promoter. Briefly, a fragment containing 1 kb of *mid2* 5' UTR and the different *mid2* fragments were amplified from genomic DNA purified from a wild type strain and cloned between *KpnI* and *NotI* sites of pSR2 (pJK148 - Pcdr2-cdr2-GFP-Tnmt1) (Keeney and Boeke, 1994). The plasmids obtained were circularized by *NruI* or *Tth111* digestion to allow integration in the *leu1* locus of a wild type strain.

A construct expressing the PH domain of Mid2 (582-685 aa) was integrated into the *leu1* locus under the control of their own promoter. Briefly, a fragment containing 1 kb of *mid2* 5` UTR and the *mid2* fragmennt coding for the PH domain of Mid2 (582-685aa) were amplified from genomic DNA purified from a wild type strain and cloned between *KpnI* and *NotI* sites of pSR98 (pJK148 Pcdr2-Cdr2-13xMyc-Tnmt1) (Rincon et al., 2014). The plasmid obtained was circularized by *NruI* digestion to allow integration in the *leu1* locus of a wild type strain.

To create the strains expressing Spn1-conGFP (*spn1-msfGFPΔN12)*, the msfGFP sequence was first amplified from plasmid pEX-A128-msfGFP and cloned into the pFA6a-EGFP-kanMX6 plasmid (Bahler et al., 1998), replacing the original EGFP for msfGFP using the Gibson Assembly cloning strategy. msfGFPΔN12 and *spn1* were amplified and fused by PCR and the PCR product was used to replace msfGFP in the pFA6a-msfGFP-kanMX6 plasmid. This construct was amplified with long oligos containing 80 pb from *spn1* 5' UTR and 3' UTR to direct homologous recombination, releasing the integration module which was used to transform wild type, *mid2Δ* and *nda3-KM-311* strains to replace *spn1* with *spn1-msfGFPΔN12*. A similar strategy was used to create the strains expressing Spn4-conGFP (*spn4ΔC6-ΔN7mEGFP)*.

All plasmids were checked by diagnostic PCR and restriction enzyme digestion, and the DNA fragments amplified by PCR were sequenced.

Microscopy and image analysis

Cells were grown at 25°C in YE5S except for cell cycle temperature sensitive (ts) mutants (*cdc7-24, sid2-250, its3-1,*), which were grown for 3 hours at 36°C or *nda3-KM311* cold sensitive (cs) mutants, which were grown up to 7h at 18°C.

Epifluorescence images were taken on a DMRXA2 upright microscope (Leica Microsystems), equipped with a 100×/1.4NA oil immersion PlanApo objective and a

Coolsnap HQ CCD camera (Photometrics), exposure time: 2 s for GFP, 1s for mCherry and 100 ms for DIC light. Quantification in the *nda3-KM311* mutant of Spn1-GFP with respect to the red markers signal was performed by intensity analysis along a line drawn throughout the cell length (dashed lines in Fig 4A and Fig S2A and B). The average values obtained were background-substracted in the same way using an equivalent region outside the cell. The curves obtained were then centered according to the position of the ring.

For time lapse imaging, 1 ml of exponentially growing cells were harvested after a centrifugation of 60 s for 800 g in a Minispin Eppendorf centrifuge equipped with a F-45-12-11 rotor, the supernatant was discarded and 1 µl of the cells was deposited in a 2% YE5S agar pad at the center of PDMS slide chambers prepared as described in ((Costa et al., 2013)).

Time-lapse movies were performed on an inverted spinning disk confocal microscope (Roper/Nikon), equipped with a Plan Apochromat 100×/1.4 NA objective lens (Nikon), a PIFOC (perfect image focus) objective stepper, and a charge-coupled device camera (EMCCD 512x512 QuantEM; Photometrics). To analyze Spn1-GFP Rlc1-mCherry Sid4-mCherry wild type as well as Mid2-ENVY Rlc1-mCherry Sid4-mCherry together with the respective cell cycle ts and cs mutants, z-stacks of 7 planes spaced by 1 µm were acquired every 1 min for 3h (binning 1, 300 EM gain; 200 ms exposure for each channel).

Fluorescent images for each channel were scaled equivalently to their respective control and analyzed using MetaMorph software 7.7.8.

Analysis of Spn1-GFP and Mid2-ENVY signals were quantified from the time of mitotic entry (SPBs separation) by measuring the average fluorescence intensity of the medial region using a linescan (Metamorph software 7.7.8) of 5 µm in length and 13µm in width oriented perpendicular to the long axis of the cell on maximum intensity projection images. Background values, measured as the average intensity of an equivalent region outside of the cell, were then subtracted.

To compare the width of Spn1-GFP and Mid2-ENVY at the two different time points indicated in the text in control and mutant cells, the linescan tool (MetaMorph software 7.7.8.) was oriented parallel to the long axis of the cell. The values obtained

derive from the average of 3 measurements over the cell width within the band corresponding to Spn1-GFP or Mid2-ENVY.

Co-immunoprecipitation experiments

Co-immunoprecipations experiments were performed as described in ((Guzman-Vendrell et al., 2013)). Briefly, 200 ml of cells were grown to an optical density at 600 nm of 1 at 25°C in YE5S medium concentrated 2 times compared to regular YE5S medium (YE5S2X) and were resuspended in 300 µl of NP40 buffer. Extracts were incubated with anti-mouse IgG magnetic beads (M-280 DYNAL, Invitrogen), coupled to 6 µg of anti-GFP mAb (Roche).

Western blots were probed with anti-GFP mAb (1/500, Roche Cat No. 11814460001) or anti-myc mAb 9E10 (1/666, Roche Cat No. 11667149001). Secondary antibodies were coupled to peroxydase (Jackson Immunoresearch).

For *nda3-KM311* synchronization experiments, 1 liter of culture was grown overnight to an optical density of 0.6. Cells were synchronized by 8 hours incubation at 18°C before being processed.

Septin-GFP fusions for orientation measurements

The Spn1-GFP fusion used throughout this study includes a flexible linker (RIPGLI) between the Spn1 and the GFP rendering this fusion not usable for orientation measurements (Fig S5A). To generate fusions of septins with rotationally constrained GFP (conGFP) we generated and screened C-terminal GFP fusions of Spn1 and Spn4 where there was no linker sequence between the septin and the GFP, and with the C-termini of septins and the N-terminus of GFP truncated to different extents, indicated as δC and ΔN, respectively. The coiled-coil prediction algorithm COILS was used to identify the ends of the predicted coiled-coils in Spn1 and Spn4 and guide the C-terminal truncations. We started with Spn1 fusions to monomeric EGFP (mEGFP) generating Spn1δC5-mEGFPΔN5 (Spn1 1-464; mEGFP starting at EELF), Spn1δC5-mEGFPΔN6, Spn1δC5-mEGFPΔN7 and Spn1δC5-mEGFPΔN11; the first three fusions behaved normally localization- and septation-wise, but the GFP was still flexible, whereas the last one was not fluorescent. Further trimming of the C-terminus to

generate Spn1δC12-mEGFPΔN5, Spn1δC12-mEGFPΔN6 and Spn1δC12-mEGFPΔN7 led to ectopic cytoplasmic bar-like structures (like the ones shown in FigS5 D). We thus turned to monomeric superfolder GFP (msfGFP) which tolerates more extensive N-terminal truncations, and generated a fusion of full-length Spn1 to msfGFP without using a linker and additionally removing residues before the first stave of the GFP β-barrel to obtain Spn1-msfGFPΔN12 (Spn1 1-469; msfGFP starting at VPILV). Spn1-msfGFPΔN12, designated as Spn1-conGFP in this study, was rotationally constrained and was used for orientation measurements. We also generated Spn4 fusions to mEGFP to obtain Spn4δC6-mEGFPΔN5 (Spn4 1-374; EGFP starting at EELF), Spn4δC6-mEGFPΔN6, Spn4δC6-mEGFPΔN7 and Spn4δC6-mEGFPΔN11. The first two constructs behaved normally, the third one formed ectopic cytoplasmic bar-like structures in addition to its localization in septin rings (Fig S5D), whereas the last one was not fluorescent. The GFP in Spn4δC6-mEGFPΔN7 was rotationally constrained and this fusion, designated as Spn4-conGFP in this study, was used to infer the orientation of septins with respect to the GFP dipole.

Spinning-disk polarization-resolved fluorescence microscopy

Yeast cells were prepared for live polarimetry measurements as described above for live microscopy. Polarization-resolved fluorescence images were acquired on a custom-built optical setup employing a confocal spinning disk unit (CSU-X1-M1 from Yokogawa) connected to the side-port of a Perfect Focus System-equipped inverted microscope (Eclipse Ti2-E from Nikon Instruments), using a Nikon Plan Apo ×100/1.45 NA oil immersion objective lens, 488- and 561-nm Sapphire laser lines (Coherent) and an iXon Ultra 888 EMCCD camera (1024×1024 pixels, 13×13 μm pixel size, Andor, Oxford Instruments), resulting in an image pixel size of 65 nm. Polarimetry images were obtained by varying the incident linear polarization with a Pockels Cell electro-optic modulator (No 28-NP Quantum Technology) synchronized to the EMCCD camera, followed by a quarter waveplate (WPQ05M-488, Thorlabs) (Wang et al., 2013). The quality of the polarization state at the sample plane was ensured by using a compensating dichroic beamsplitter similar to the one present in the spinning disk unit (405/488/561/635 nm Quad Dichroic mirror) but placed at 90° reflection to exchange s and p polarization state phase-shifts. A polarization stack is made of 18 polarized

images using an incident linear polarization varying from 0° (correspoding to the horizontal direction in the image) to 170° with steps of 10°. The recorded stack is used to obtain the polarization response of the sample at each pixel, from which GFP orientation information can be deduced. Three to five large field-of-view images (66×66 μm) typically containing 10-20 cells during cytokinesis per image, were collected for wild-type and *nda3* cells; seven to eight such images were collected for *mid2Δ* cells to account for the smaller number of *mid2Δ* dividing cells per field of view. An exposure time of 0.5 s was used per image. Before each polarimetry measurement, a two-color z-stack was acquired (Δz = 1.0 μm) to image both septin-GFP fusions and myosin/spindle bodies; these images were used for staging the measured cells and correlating the measured orientation distributions with the different stages of cytokinesis. A polarization stack was then recorded for each position within a z-stack (Δz = 1.0 μm) for the septin-GFP channel, and thus allowed to obtain polarimetry images throughout the septin rings, containing both tangential-most views where the entirety of the ring can be seen parallel to the xy plane, and more equatorial views showing cross-sections that appear as spots on either side of the ring. To minimize bias in the measured orientations due to the contribution of off-plane orientations we focused on the tangential-most views, as shown in Fig 5 and Fig S5.

Polarization stack images were first processed with the open-source image processing software ImageJ/Fiji. Images within each polarization stack were systematically registered using the StackReg plugin to correct for drift during the acquisition. The proper z planes, i.e. the ones containing the tangential-most views of the ring, were then identified for each cell, and polarimetry data were analyzed according to the framework defined by (Kress et al., 2013) to obtain the mean GFP dipole orientation (angle ρ) per pixel. Analysis and data representation, including color-coded stick representations of the measured orientations per pixel and polar-plot histograms, were done using the Polarimetry Analysis software which is a Matlab App Designer standalone application. The source code is available at gitHub.com/cchandre/Polarimetry, and the desktop app can be freely obtained at https://www.fresnel.fr/polarimetry under a BSD license.

The regions of interest for analysis were selected by a combination of intensity thresholding and manual selection of the features to analyze. Each region of interest

contained typically 120-200 analyzed pixels i.e. 120-200 orientation color-coded sticks in the tangential-most view of the septin ring per cell (Fig 5 and Fig S5). The mean orientation per pixel is represented as a stick whose orientation and color are the measured angle ρ within the resolution limit of the microscope (~200 nm). The distribution of mean orientations was represented in 0-180°polar-plot histograms. To assess the extent to which the measured orientations were more parallel or more perpendicular with respect to the CR ring axis, the ring axis angle in each cell was used to normalize the angle distributions from 0-180° to 0-90° and generate 0-90° polar plots (Fig 5 and Fig S5), with 0° and 90° defining orientations parallel and perpendicular to the ring axis, respectively. To facilitate the visual comparison of orientation distributions between cells and also relate directly to the 0-90° polar plots, representative cells in Fig 5 and Fig S5 have been rotated using the Polarimetry Analysis software so that their CR axes correspond to the horizontal orientations (0°). 0-90° normalized polar-plot histograms from all cells in a given condition were concatenated to represent all analyzed data in each condition, were rescaled to their respective maximum value to facilitate comparisons, and orientations sorted in bins of 6°. The normalization of orientation distributions with respect to the CR ring axis, the normalization of 0-180° to 0-90° polar plots and the rescaling of histograms were done with custom-generated Matlab codes, the source codes of which are available at gitHub.com/cchandre/Polarimetry.

Statistical analysis

Sample size (n) is defined in each figure and derived from 3 independent experiments, except for the co-immunoprecipitations assays in Figure S3, which were repeated twice. The error bars correspond standard deviation (SD) between experiments and are specifically indicated in each figure.

SUPPLEMENTAL INFORMATION

Supplemental information includes seven figures and one table.

ACKNOWLEDGEMENTS

We thank Vincent Fraisier for maintenance of the microscopes for imaging performed on the Institut Curie, Paris (PICT-IBISA, part of France-Bioimaging national research infrastructure), Carmen Castro for maintenance of the microscopes performed on IBFG (Salamanca, Spain) andCristel Chandre (I2M, CNRS, Marseille, France) for the Polarimetry Analysis app and Matlab codes used for polarimetry data analysis. We also wish to thank to Pilar Pérez and Carlos Rodríguez for their very helpful comments on the manuscript. This work was supported by a grant from Fondation ARC to A.P. Federica Arbizzani received a fourth year PhD fellowship from Fondation ARC. AP is a member of the LabEx CelTisPhyBio. S.A.R. is a Ramon y Cajal fellow of the University of Salamanca. This work is supported by the Agence Nationale de la Recherche, Fondation ARC pour la Recherche sur le Cancer, the MICINN grant PGC2018-094090-B-I00, and "Escalera de Excelencia" CLU-2017-03 and the Agence Nationale pour la Recherche (ANR grant ANR-17-CE13-0014; SEPTIMORF). The authors declare no competing financial interests.

AUTHOR CONTRIBUTIONS

Federica Arbizzani performed the experiments analyzed the data and wrote the manuscript. Manos Mavrakis and Sophie Brasselet performed the polarization microscopy experiments and edited the manuscript. Anne Paoletti and Sergio Rincon directed the study and edited the manuscript.

REFERENCES

AN, H., MORRELL, J. L., JENNINGS, J. L., LINK, A. J. & GOULD, K. L. 2004. Requirements of fission yeast septins for complex formation, localization, and function. *Mol Biol Cell,* 15**,** 5551-64.

BAHLER, J., WU, J. Q., LONGTINE, M. S., SHAH, N. G., MCKENZIE, A., 3RD, STEEVER, A. B., WACH, A., PHILIPPSEN, P. & PRINGLE, J. R. 1998. Heterologous modules for efficient and versatile PCR-based gene targeting in Schizosaccharomyces pombe. *Yeast,* 14**,** 943-51.

BALASUBRAMANIAN, M. K., MCCOLLUM, D., CHANG, L., WONG, K. C., NAQVI, N. I., HE, X., SAZER, S. & GOULD, K. L. 1998. Isolation and characterization of new fission yeast cytokinesis mutants. *Genetics,* 149**,** 1265-75.

BERLIN, A., PAOLETTI, A. & CHANG, F. 2003a. Mid2 stabilizes septin rings during cytokinesis in fission yeast. *JCB* 160**,** 1083-1092.
BERLIN, A., PAOLETTI, A. & CHANG, F. 2003b. Mid2p stabilizes septin rings during cytokinesis in fission yeast. *J Cell Biol,* 160**,** 1083-92.
BERTIN, A., MCMURRAY, M. A., THAI, L., GARCIA, G., 3RD, VOTIN, V., GROB, P., ALLYN, T., THORNER, J. & NOGALES, E. 2010. Phosphatidylinositol-4,5-bisphosphate promotes budding yeast septin filament assembly and organization. *J Mol Biol,* 404**,** 711-31.
BHAVSAR-JOG, Y. P. & BI, E. 2017. Mechanics and regulation of cytokinesis in budding yeast. *Semin Cell Dev Biol,* 66**,** 107-118.
BRIDGES, A. A. & GLADFELTER, A. S. 2015. Septin Form and Function at the Cell Cortex. *J Biol Chem,* 290**,** 17173-80.
BRIDGES, A. A., JENTZSCH, M. S., OAKES, P. W., OCCHIPINTI, P. & GLADFELTER, A. S. 2016. Micron-scale plasma membrane curvature is recognized by the septin cytoskeleton. *J Cell Biol,* 213**,** 23-32.
BRIDGES, A. A., ZHANG, H., MEHTA, S. B., OCCHIPINTI, P., TANI, T. & GLADFELTER, A. S. 2014. Septin assemblies form by diffusion-driven annealing on membranes. *Proc Natl Acad Sci U S A,* 111**,** 2146-51.
CAUVIN, C. & ECHARD, A. 2015. Phosphoinositides: Lipids with informative heads and mastermind functions in cell division. *Biochim Biophys Acta,* 1851**,** 832-43.
CAVISTON, J. P., LONGTINE, M., PRINGLE, J. R. & BI, E. 2003. The role of Cdc42p GTPase-activating proteins in assembly of the septin ring in yeast. *Mol Biol Cell,* 14**,** 4051-66.
COSTA, J., FU, C., SYROVATKINA, V. & TRAN, P. T. 2013. Imaging individual spindle microtubule dynamics in fission yeast. *Methods Cell Biol,* 115**,** 385-94.
DEMAY, B. S., BAI, X., HOWARD, L., OCCHIPINTI, P., MESEROLL, R. A., SPILIOTIS, E. T., OLDENBOURG, R. & GLADFELTER, A. S. 2011a. Septin filaments exhibit a dynamic, paired organization that is conserved from yeast to mammals. *J Cell Biol,* 193**,** 1065-81.
DEMAY, B. S., NODA, N., GLADFELTER, A. S. & OLDENBOURG, R. 2011b. Rapid and quantitative imaging of excitation polarized fluorescence reveals ordered septin dynamics in live yeast. *Biophys J,* 101**,** 985-94.
DOBBELAERE, J. & BARRAL, Y. 2004. Spatial coordination of cytokinetic events by compartmentalization of the cell cortex. *Science,* 305**,** 393-6.
DOBBELAERE, J., GENTRY, M. S., HALLBERG, R. L. & BARRAL, Y. 2003. Phosphorylation-dependent regulation of septin dynamics during the cell cycle. *Dev Cell,* 4**,** 345-57.
ECHARD, A., HICKSON, G. R., FOLEY, E. & O'FARRELL, P. H. 2004. Terminal cytokinesis events uncovered after an RNAi screen. *Curr Biol,* 14**,** 1685-93.
EL AMINE, N., KECHAD, A., JANANJI, S. & HICKSON, G. R. 2013. Opposing actions of septins and Sticky on Anillin promote the transition from contractile to midbody ring. *J Cell Biol,* 203**,** 487-504.
ELUERE, R., VARLET, I., BERNADAC, A. & SIMON, M. N. 2012. Cdk and the anillin homolog Bud4 define a new pathway regulating septin organization in yeast. *Cell Cycle,* 11**,** 151-8.
FIELD, C. M., COUGHLIN, M., DOBERSTEIN, S., MARTY, T. & SULLIVAN, W. 2005. Characterization of anillin mutants reveals essential roles in septin localization and plasma membrane integrity. *Development,* 132**,** 2849-60.
FOUNOUNOU, N., LOYER, N. & LE BORGNE, R. 2013. Septins regulate the contractility of the actomyosin ring to enable adherens junction remodeling during cytokinesis of epithelial cells. *Dev Cell,* 24**,** 242-55.
FU, C., WARD, J. J., LOIODICE, I., VELVE-CASQUILLAS, G., NEDELEC, F. J. & TRAN, P. T. 2009. Phospho-regulated interaction between kinesin-6 Klp9p and microtubule bundler Ase1p promotes spindle elongation. *Dev Cell,* 17**,** 257-67.
FUJIWARA, T., BANDI, M., NITTA, M., IVANOVA, E. V., BRONSON, R. T. & PELLMAN, D. 2005. Cytokinesis failure generating tetraploids promotes tumorigenesis in p53-null cells. *Nature,* 437**,** 1043-7.

GLADFELTER, A. S., PRINGLE, J. R. & LEW, D. J. 2001. The septin cortex at the yeast mother-bud neck. *Curr Opin Microbiol,* 4**,** 681-9.
GUZMAN-VENDRELL, M., BALDISSARD, S., ALMONACID, M., MAYEUX, A., PAOLETTI, A. & MOSELEY, J. B. 2013. Blt1 and Mid1 provide overlapping membrane anchors to position the division plane in fission yeast. *Mol Cell Biol,* 33**,** 418-28.
HAGAN, I. & YANAGIDA, M. 1990. Novel potential mitotic motor protein encoded by the fission yeast cut7+ gene. *Nature,* 347**,** 563-6.
HAGAN, I. & YANAGIDA, M. 1992. Kinesin-related cut7 protein associates with mitotic and meiotic spindles in fission yeast. *Nature,* 356**,** 74-6.
HARTWELL, L. H. 1971. Genetic control of the cell division cycle in yeast. II. Genes controlling DNA replication and its initiation. *J Mol Biol,* 59**,** 183-94.
HERGOVICH, A., STEGERT, M. R., SCHMITZ, D. & HEMMINGS, B. A. 2006. NDR kinases regulate essential cell processes from yeast to humans. *Nat Rev Mol Cell Biol,* 7**,** 253-64.
HICKSON, G. R. & O'FARRELL, P. H. 2008. Anillin: a pivotal organizer of the cytokinetic machinery. *Biochem Soc Trans,* 36**,** 439-41.
JIN, Q. W., ZHOU, M., BIMBO, A., BALASUBRAMANIAN, M. K. & MCCOLLUM, D. 2006. A role for the septation initiation network in septum assembly revealed by genetic analysis of sid2-250 suppressors. *Genetics,* 172**,** 2101-12.
JUANES, M. A. & PIATTI, S. 2016. The final cut: cell polarity meets cytokinesis at the bud neck in S. cerevisiae. *Cell Mol Life Sci,* 73**,** 3115-36.
KANG, P. J., HOOD-DEGRENIER, J. K. & PARK, H. O. 2013. Coupling of septins to the axial landmark by Bud4 in budding yeast. *J Cell Sci,* 126**,** 1218-26.
KECHAD, A., JANANJI, S., RUELLA, Y. & HICKSON, G. R. 2012. Anillin acts as a bifunctional linker coordinating midbody ring biogenesis during cytokinesis. *Curr Biol,* 22**,** 197-203.
KINOSHITA, M., FIELD, C. M., COUGHLIN, M. L., STRAIGHT, A. F. & MITCHISON, T. J. 2002. Self- and actin-templated assembly of Mammalian septins. *Dev Cell,* 3**,** 791-802.
KOZUBOWSKI, L., LARSON, J. R. & TATCHELL, K. 2005. Role of the septin ring in the asymmetric localization of proteins at the mother-bud neck in Saccharomyces cerevisiae. *Mol Biol Cell,* 16**,** 3455-66.
KRESS, A., WANG, X., RANCHON, H., SAVATIER, J., RIGNEAULT, H., FERRAND, P. & BRASSELET, S. 2013. Mapping the local organization of cell membranes using excitation-polarization-resolved confocal fluorescence microscopy. *Biophys J,* 105**,** 127-36.
LACROIX, B. & MADDOX, A. S. 2012. Cytokinesis, ploidy and aneuploidy. *J Pathol,* 226**,** 338-51.
LEE, I. J., COFFMAN, V. C. & WU, J. Q. 2012. Contractile-ring assembly in fission yeast cytokinesis: Recent advances and new perspectives. *Cytoskeleton (Hoboken),* 69**,** 751-63.
LIU, J., FAIRN, G. D., CECCARELLI, D. F., SICHERI, F. & WILDE, A. 2012. Cleavage furrow organization requires PIP(2)-mediated recruitment of anillin. *Curr Biol,* 22**,** 64-9.
LIU, J., WANG, H. & BALASUBRAMANIAN, M. K. 2000. A checkpoint that monitors cytokinesis in Schizosaccharomyces pombe. *J Cell Sci,* 113 (Pt 7)**,** 1223-30.
MARQUARDT, J., CHEN, X. & BI, E. 2019. Architecture, remodeling, and functions of the septin cytoskeleton. *Cytoskeleton (Hoboken),* 76**,** 7-14.
MARTIN-CUADRADO, A. B., MORRELL, J. L., KONOMI, M., AN, H., PETIT, C., OSUMI, M., BALASUBRAMANIAN, M., GOULD, K. L., DEL REY, F. & DE ALDANA, C. R. 2005. Role of septins and the exocyst complex in the function of hydrolytic enzymes responsible for fission yeast cell separation. *Mol Biol Cell,* 16**,** 4867-81.
MCCOLLUM, D. & GOULD, K. L. 2001. Timing is everything: regulation of mitotic exit and cytokinesis by the MEN and SIN. *Trends Cell Biol,* 11**,** 89-95.
MCMURRAY, M. A. & THORNER, J. 2009. Septins: molecular partitioning and the generation of cellular asymmetry. *Cell Div,* 4**,** 18.

MCQUILKEN, M., JENTZSCH, M. S., VERMA, A., MEHTA, S. B., OLDENBOURG, R. & GLADFELTER, A. S. 2017. Analysis of Septin Reorganization at Cytokinesis Using Polarized Fluorescence Microscopy. *Front Cell Dev Biol,* 5**,** 42.

MEITINGER, F. & PALANI, S. 2016. Actomyosin ring driven cytokinesis in budding yeast. *Semin Cell Dev Biol,* 53**,** 19-27.

MORENO, S., KLAR, A. & NURSE, P. 1991. Molecular genetic analysis of fission yeast Schizosaccharomyces pombe. *Methods Enzymol,* 194**,** 795-823.

MOSTOWY, S. & COSSART, P. 2012. Septins: the fourth component of the cytoskeleton. *Nat Rev Mol Cell Biol,* 13**,** 183-94.

NEUFELD, T. P. & RUBIN, G. M. 1994. The Drosophila peanut gene is required for cytokinesis and encodes a protein similar to yeast putative bud neck filament proteins. *Cell,* 77**,** 371-9.

OEGEMA, K., SAVOIAN, M. S., MITCHISON, T. J. & FIELD, C. M. 2000. Functional analysis of a human homologue of the Drosophila actin binding protein anillin suggests a role in cytokinesis. *J Cell Biol,* 150**,** 539-52.

ONG, K., WLOKA, C., OKADA, S., SVITKINA, T. & BI, E. 2014. Architecture and dynamic remodelling of the septin cytoskeleton during the cell cycle. *Nat Commun,* 5**,** 5698.

PIEKNY, A. J. & GLOTZER, M. 2008. Anillin is a scaffold protein that links RhoA, actin, and myosin during cytokinesis. *Curr Biol,* 18**,** 30-6.

PIEKNY, A. J. & MADDOX, A. S. 2010. The myriad roles of Anillin during cytokinesis. *Semin Cell Dev Biol,* 21**,** 881-91.

POLLARD, T. D. & WU, J. Q. 2010. Understanding cytokinesis: lessons from fission yeast. *Nat Rev Mol Cell Biol,* 11**,** 149-55.

RINCON, S. A., BHATIA, P., BICHO, C., GUZMAN-VENDRELL, M., FRAISIER, V., BOREK, W. E., ALVES FDE, L., DINGLI, F., LOEW, D., RAPPSILBER, J., SAWIN, K. E., MARTIN, S. G. & PAOLETTI, A. 2014. Pom1 regulates the assembly of Cdr2-Mid1 cortical nodes for robust spatial control of cytokinesis. *J Cell Biol,* 206**,** 61-77.

RINCON, S. A. & PAOLETTI, A. 2012. Mid1/anillin and the spatial regulation of cytokinesis in fission yeast. *Cytoskeleton (Hoboken),* 69**,** 764-77.

RINCON, S. A. & PAOLETTI, A. 2016. Molecular control of fission yeast cytokinesis. *Semin Cell Dev Biol,* 53**,** 28-38.

SAARIKANGAS, J. & BARRAL, Y. 2011. The emerging functions of septins in metazoans. *EMBO Rep,* 12**,** 1118-26.

SINHA, I., WANG, Y. M., PHILP, R., LI, C. R., YAP, W. H. & WANG, Y. 2007. Cyclin-dependent kinases control septin phosphorylation in Candida albicans hyphal development. *Dev Cell,* 13**,** 421-32.

SLUBOWSKI, C. J., FUNK, A. D., ROESNER, J. M., PAULISSEN, S. M. & HUANG, L. S. 2015. Plasmids for C-terminal tagging in Saccharomyces cerevisiae that contain improved GFP proteins, Envy and Ivy. *Yeast,* 32**,** 379-87.

SOMMA, M. P., FASULO, B., CENCI, G., CUNDARI, E. & GATTI, M. 2002. Molecular dissection of cytokinesis by RNA interference in Drosophila cultured cells. *Mol Biol Cell,* 13**,** 2448-60.

SPARKS, C. A., MORPHEW, M. & MCCOLLUM, D. 1999. Sid2p, a spindle pole body kinase that regulates the onset of cytokinesis. *J Cell Biol,* 146**,** 777-90.

STORCHOVA, Z. & PELLMAN, D. 2004. From polyploidy to aneuploidy, genome instability and cancer. *Nat Rev Mol Cell Biol,* 5**,** 45-54.

STRAIGHT, A. F., FIELD, C. M. & MITCHISON, T. J. 2005. Anillin binds nonmuscle myosin II and regulates the contractile ring. *Mol Biol Cell,* 16**,** 193-201.

SURKA, M. C., TSANG, C. W. & TRIMBLE, W. S. 2002. The mammalian septin MSF localizes with microtubules and is required for completion of cytokinesis. *Mol Biol Cell,* 13**,** 3532-45.

TASTO, J. J., MORRELL, J. L. & GOULD, K. L. 2003. An anillin homologue, Mid2p, acts during fission yeast cytokinesis to organize the septin ring and promote cell separation. *J Cell Biol,* 160**,** 1093-103.

VERSELE, M. & THORNER, J. 2005. Some assembly required: yeast septins provide the instruction manual. *Trends Cell Biol,* 15**,** 414-24.

VRABIOIU, A. M. & MITCHISON, T. J. 2006. Structural insights into yeast septin organization from polarized fluorescence microscopy. *Nature,* 443**,** 466-9.

WANG, X., KRESS, A., BRASSELET, S. & FERRAND, P. 2013. High frame-rate fluorescence confocal angle-resolved linear dichroism microscopy. *Rev Sci Instrum,* 84**,** 053708.

WOOD, V., GWILLIAM, R., RAJANDREAM, M. A., LYNE, M., LYNE, R., STEWART, A., SGOUROS, J., PEAT, N., HAYLES, J., BAKER, S., BASHAM, D., BOWMAN, S., BROOKS, K., BROWN, D., BROWN, S., CHILLINGWORTH, T., CHURCHER, C., COLLINS, M., CONNOR, R., CRONIN, A., DAVIS, P., FELTWELL, T., FRASER, A., GENTLES, S., GOBLE, A., HAMLIN, N., HARRIS, D., HIDALGO, J., HODGSON, G., HOLROYD, S., HORNSBY, T., HOWARTH, S., HUCKLE, E. J., HUNT, S., JAGELS, K., JAMES, K., JONES, L., JONES, M., LEATHER, S., MCDONALD, S., MCLEAN, J., MOONEY, P., MOULE, S., MUNGALL, K., MURPHY, L., NIBLETT, D., ODELL, C., OLIVER, K., O'NEIL, S., PEARSON, D., QUAIL, M. A., RABBINOWITSCH, E., RUTHERFORD, K., RUTTER, S., SAUNDERS, D., SEEGER, K., SHARP, S., SKELTON, J., SIMMONDS, M., SQUARES, R., SQUARES, S., STEVENS, K., TAYLOR, K., TAYLOR, R. G., TIVEY, A., WALSH, S., WARREN, T., WHITEHEAD, S., WOODWARD, J., VOLCKAERT, G., AERT, R., ROBBEN, J., GRYMONPREZ, B., WELTJENS, I., VANSTREELS, E., RIEGER, M., SCHAFER, M., MULLER-AUER, S., GABEL, C., FUCHS, M., DUSTERHOFT, A., FRITZC, C., HOLZER, E., MOESTL, D., HILBERT, H., BORZYM, K., LANGER, I., BECK, A., LEHRACH, H., REINHARDT, R., POHL, T. M., EGER, P., ZIMMERMANN, W., WEDLER, H., WAMBUTT, R., PURNELLE, B., GOFFEAU, A., CADIEU, E., DREANO, S., GLOUX, S., et al. 2002. The genome sequence of Schizosaccharomyces pombe. *Nature,* 415**,** 871-80.

WU, H., GUO, J., ZHOU, Y. T. & GAO, X. D. 2015. The anillin-related region of Bud4 is the major functional determinant for Bud4's function in septin organization during bud growth and axial bud site selection in budding yeast. *Eukaryot Cell,* 14**,** 241-51.

WU, J. Q., KUHN, J. R., KOVAR, D. R. & POLLARD, T. D. 2003. Spatial and temporal pathway for assembly and constriction of the contractile ring in fission yeast cytokinesis. *Dev Cell,* 5**,** 723-34.

ZHAO, W. M. & FANG, G. 2005. Anillin is a substrate of anaphase-promoting complex/cyclosome (APC/C) that controls spatial contractility of myosin during late cytokinesis. *J Biol Chem,* 280**,** 33516-24.

ZHENG, S., DONG, F., RASUL, F., YAO, X., JIN, Q. W., ZHENG, F. & FU, C. 2018. Septins regulate the equatorial dynamics of the separation initiation network kinase Sid2p and glucan synthases to ensure proper cytokinesis. *FEBS J,* 285**,** 2468-2480.

ABBREVIATIONS

CR: Contractile Ring

SIN: Septation Initiation Network

CDK: Cyclin-Dependent Kinase

FIGURE LEGENDS

Figure 1: Dynamics of septins and Mid2 during cell division

Time lapse imaging of wild type cells expressing Spn1-GFP, Rlc1-mCherry and Sid4-m Cherry (**A**) or Mid2-ENVY, Rlc1-mCherry and Sid4-mCherry (**B**) grown at 25°C. Maximum intensity projections of confocal images are shown. Time 0 corresponds to mitotic entry. Scale bars: 2 µm. **C:** Kymographs showing the medial region of the cell expressing Spn1-GFP Rlc1-mCherry (left) or Mid2-ENVY Rlc1-mCherry (right). There is a 1-minute interval between successive images. The major transitions in the behavior of Spn1 and Mid2 are highlighted at the far right, in bigger panels and indicated with a star (color code matches that of the graph in D). **D:** Plot depicting the timing of Spn1-GFP transitions throughout cell division. The indicated times correspond to the starting times of each transition, using SPB separation as a timer for mitotic entry (t=0 in A). Mean ± sd are shown. n=51 cells. **E:** Plot showing the dynamics of Mid2-ENVY throughout cell division. Mean ± sd are shown. n=51 cells. **F:** Analysis of Spn1-GFP (light green) and Mid2-ENVY (dark green) intensities from mitotic onset throughout cell division. The average curves ± sd are displayed. n=6 cells. **G:** Quantification of the extent of Spn1-GFP (light green) and Mid2-ENVY (dark green) width compaction over time. n=30 cells

Figure 2: Defects in septins behavior in the absence of Mid2

Time lapse imaging of wild type (**A**) and *mid2Δ* cells (**B**) expressing Spn1-GFP, Rlc1-mCherry and Sid4-mCherry grown at 25°C. Maximum intensity projections of confocal

images are shown. Time 0 corresponds to mitotic entry. Scale bars: 2 µm. **C:** Kymographs showing the medial region of wild type (left) or *mid2Δ* cells (right) expressing Spn1-GFP, Rlc1-mCherry and Sid4-mCherry. Frame are spaced by 1 min intervals. The major transitions in Spn1-GFP dynamics and the defects observed in absence of *mid2* are highlighted in bigger panels at the far right and indicated with a star (color code matches that of the graph in D). **D:** Plot displaying the dynamics of Spn1-GFP throughout cell division. Mean ± sd are shown. n=52 cells. **E:** Plot showing the dynamics of Spn1-GFP in *mid2Δ* cells during cytokinesis. Mean ± sd are shown. n=52 cells. **F:** Analysis of Spn1-GFP intensity in wild type (green) and in *mid2Δ* cells (orange) from mitotic onset throughout cell division. The average curves ± sd are displayed. n=6 cells. **G:** Quantification of the extent of Spn1-GFP width compaction over time in wild type (green) and in *mid2Δ* cells (orange). n=20 cells.

Figure 3: Mid2 interacts with other Mid2 molecules through different regions of the protein

A: Co-immunoprecipitation assay between Mid2-13Myc and full length Mid2-GFP or Mid2ΔPH-GFP in presence (*spn1⁺*) or absence of Spn1 (*spn1Δ*). Black asterisks show immunoglobulin bands; red asterisks show the expected Mid2 bands. Additional bands may represent degradation products of Mid2. **B:** Co-immunoprecipitation assay between the PH domain of Mid2 tagged with 13XMyc and the PH domain of Mid2 tagged with GFP in the presence (*spn1⁺*) or absence of Spn1 (*spn1Δ*). Black asterisks show immunoglobulin bands; red asterisks show the expected Mid2-PH bands. **C:** Diagram showing the structure of the anillin-like protein Mid2 with the main domains highlighted.

Figure 4: Septins accumulate as a broad band at the cell middle under high CDK activity

A: Epifluorescence images of cells expressing Spn1-GFP Rlc1-mCherry Sid4-mCherry (left panels) or Mid2-ENVY Rlc1-mCherry Sid4-mCherry (right panels) in wild type or *nda3-KM311* cells growing at 18°C during 4 hours. Fluorescence intensity analysis of Spn1-GFP, Rlc1-mCherry and Sid4-mCherry signals along the entire cell length of *nda3-KM311* cells incubated during 7 hours at 18°C. n=10 cells (far right panel). Time lapse

imaging of wild type (**B**) or *cut7-24* cells (**D**) expressing Spn1-GFP, Rlc1-mCherry and Sid4-mCherry grown at 36°C. Maximum intensity projections of confocal images are shown. Time 0 corresponds to mitotic entry. Scale bars: 2 µm. Plot showing Spn1-GFP transitions throughout cell division in the wild type (**C**) or the *cut7-24* mutant (**E**). Mean ± sd are shown. n=45 cells in each case. **F:** Quantification of the extent of Spn1-GFP width compaction over the time in wild type (green) and in *cut7-24* cells (red). n=20 cells.

Figure 5: Septin filament organization changes during CR assembly and constriction, and depends on Mid2

A: Polar-plot histograms of GFP dipole orientations of Spn1-conGFP filaments from wild type cells at different stages of cytokinesis (top panels). The number of analyzed cells per stage is indicated below each polar-plot histogram (typically 120-200 analyzed pixels per cell). Confocal images of Spn1-conGFP from selected wild type cells (grayscale images) and an overlaid color-coded stick representation of the measured orientations (angles ρ) per analyzed pixel at each cytokinetic stage (bottom panels). Scale bar: 1 µm. **B**: Polar plots of GFP dipole orientations of Spn1-conGFP filaments from *mid2Δ* cells at different stages of cytokinesis (top panels). The number of analyzed cells per stage is indicated below each polar-plot histogram. Confocal images of Spn1-conGFP from selected *mid2Δ* cells (grayscale images) and an overlaid color-coded stick representation of the measured orientations per pixel, as in A, at each cytokinetic stage (bottom panels). Scale bar: 1 µm. **C:** Polar plot of GFP dipole orientations of Spn1-conGFP filaments from 57 *nda3-KM311* cells incubated 7 hours at 18°C (top panel). Confocal images of Spn1-conGFP from *nda3-KM311* cells (grayscale images) and an overlaid color-coded stick representation of the measured orientations per pixel, as in A (bottom panels). Scale bar: 1 µm. **D**) Schematic representation of septin localization related to major CR transitions (top) and detail of septin filament orientation at each stage (bottom). The cartoon on the bottom right depicts the orientation of a septin filament with respect to the orientation of GFP dipoles (double arrowheads), as deduced from Spn4-conGFP fusions (see Fig S5D and E). The GFP barrels orient with their long axes parallel to the septin filament axis, i.e. with the GFP

dipoles perpendicular to the septin filament axis. The numbers correspond to the septin subunits Spn1-4 and the dashed lines delimit a putative octameric septin complex within the filament. The septin subunit order is based on An et al (2004) and homology with budding yeast septins.

Figure 6: Septins show defects in recruitment and compaction under low SIN activity
Time lapse imaging of wild type (**A**) and *sid2-250* cells (**C**), expressing Spn1-GFP, Rlc1-mCherry and Sid4-mCherry incubated at 36°C. Maximum intensity projections of confocal images are shown. Time 0 corresponds to mitotic entry. Scale bars: 2 µm. Plot showing Spn1-GFP transitions throughout cell division in wild type (**B**) or *sid2-250* cells (**D**). Mean ± sd are shown. Wild type n=58 cells; *sid2-250* n=70 cells. **E:** Analysis of Spn1-GFP intensity from mitotic onset throughout cell division in control (green) and *sid2-250* cells (red). The average curves ± sd are displayed. n=6 cells. **F:** Quantification of the extent of Spn1-GFP width compaction over the time in wild type (green) and *sid2-250* cells (red). n=20 cells.

Figure 7: Septins recruitment and compaction is defective in the Bgs1 mutant *cps1-191*
Time lapse imaging of wild type (**A**) and *cps1-191* cells (**C**), expressing Spn1-GFP, Rlc1-mCherry and Sid4-mCherry incubated at 36°C. Maximum intensity projections of confocal images are shown. Time 0 corresponds to mitotic entry. Scale bars: 2 µm. Plot showing Spn1-GFP transitions throughout cell division in wild type (**B**) or *cps1-191* cells (**D**). Mean ± sd are shown. Wild type n=50 cells; *cps1-191* n=78 cells. **E:** Analysis of Spn1-GFP intensity from mitotic onset throughout cell division in control (green) and *cps1-191* cells (red). The average curves ± sd are displayed. n=6 cells. **F:** Quantification of the extent of Spn1-GFP width compaction over the time in wild type (green) and *cps1-191* cells (red). n=20 cells.

SUPPLEMENTAL INFORMATION

Table S1. Table of strains used in this study.

Strain	Genotype	Source
Figure 1		
AP5501	*spn1-GFP:kanMX6 rlc1-mCherry:natMX6 sid4-mCherry:hphMX6 ade6- ura4-D18 leu1-32*	This study
AP5678	*mid2-ENVY:kanMX6 rlc1-mCherry:natMX6 sid4-mCherry:hphMX6 ade6-M210 ura4-D18 leu1-32*	This study
Figure 2		
AP5501	*spn1-GFP:kanMX6 rlc1-mCherry:natMX6 sid4-mCherry:hphMX6 ade6- ura4-D18 leu1-32*	This study
AP5582	*spn1-GFP:kanMX6 mid2::kanMX6 rlc1-mCherry:natMX6 sid4-mCherry:hphMX6 ade6-M210 ura4-D18 leu1-32*	This study
Figure 3		
AP5823	*mid2-13xMyc:Nat ade6-M210 ura4-D18 leu1-32*	This study
AP5831	*leu1+:Pmid1-mid2-GFP mid2-13xMyc:Nat ade6-M210 ura4-D18 leu1-32*	This study
AP5829	*leu1+:Pmid1-mid2ΔPH-GFP mid2-13xMyc:Nat ade6-M210 ura4-D18 leu1-32*	This study
AP5918	*spn1::ura4+ mid2-13xMyc:Nat ade6-M210 ura4-D18 leu1-32*	This study
AP5920	*spn1::ura4+ leu1+:Pmid1-mid2-GFP mid2-13xMyc:natMX6 ade6-*	This study
AP5927	*spn1::ura4+ leu1+:Pmid1-mid2ΔPH-GFP mid2-13xMyc:natMX6 ade6-M210 ura4-D18 leu1-32*	This study
AP5814	*leu1+:Pmid1-PHmid2-13xMyc ade6-M210 ura4-D18 leu1-32*	This study
AP5932	*PHmid2-GFP:kanMX6 leu1+:Pmid1-PHmid2-13xMyc ade6-M210 ura4-D18 leu1-32*	This study
AP5930	*spn1::ura4+ leu1+:Pmid1-PHmid2-13xMyc ade6-M210 ura4-D18 leu1-32*	This study
AP5943	*spn1::ura4+ PHmid2-GFP:kanMX6 leu1+:Pmid1-PHmid2-13xMyc ade6-M210 ura4-D18 leu1-32*	This study
Figure 4		

AP5501	*spn1-GFP:kanMX6 rlc1-mCherry:natMX6 sid4-mCherry:hphMX6 ade6-M210 ura4-D18 leu1-32*	This study
AP5515	*spn1-GFP:kanMX6 rlc1-mCherry:natMX6 sid4-mCherry:hphMX6 nda3-KM311 ade6-M210 ura4-D18 leu1-32*	This study
AP6268	*spn1-GFP:kanMX6 rlc1-mCherry:natMX6 sid4-mCherry:hphMX6 cut7-24 ade6-M210 ura4-D18 leu1-32*	This study
AP5678	*mid2-ENVY:kanMX6 rlc1-mCherry:natMX6 sid4-mCherry:hphMX6 ade6-M210 ura4-D18 leu1-32*	This study
AP5514	*mid2-ENVY:kanMX6 rlc1-mCherry:natMX6 sid4-mCherry:hphMX6 nda3-KM311 ade6-M210 ura4-D18 leu1-32*	This study
Figure 5		
AP6313	*spn1-msfGFPΔN12:kanMX6 rlc1-mCherry:natMX6 sid4-mCherry:hphMX6 ade6-M210 ura4-D18 leu1-32*	This study
AP6334	*spn1-msfGFPΔN12:kanMX6 mid2::hphMX6 rlc1-mCherry:natMX6 sid4-mCherry:hphMX6 ade6-M210 ura4-D18 leu1-32*	This study
AP6324	*spn1-msfGFPΔN12:kanMX6 nda3-KM311 rlc1-mCherry:natMX6 sid4-mCherry:hphMX6 ade6-M210 ura4-D18 leu1-32*	This study
Figure 6		
AP5501	*spn1-GFP:kanMX6 rlc1-mCherry:natMX6 sid4-mCherry:hphMX6 ade6-M210 ura4-D18 leu1-32*	This study
AP5585	*spn1-GFP:kanMX6 rlc1-mCherry:natMX6 sid4-mCherry:hphMX6 sid2-250 ade6-M210 ura4-D18 leu1-32*	This study
Figure 7		
AP5501	*spn1-GFP:kanMX6 rlc1-mCherry:natMX6 sid4-mCherry:hphMX6 ade6-M210 ura4-D18 leu1-32*	This study
AP5633	*spn1-GFP:kanMX6 rlc1-mCherry:natMX6 sid4-mCherry:hphMX6 cps1-191ade6-M210 ura4-D18 leu1-32*	This study
Figure S1		
AP5501	*spn1-GFP:kanMX6 rlc1-mCherry:natMX6 sid4-mCherry:hphMX6 ade6-M210 ura4-D18 leu1-32*	This study
AP5582	*spn1-GFP:kanMX6 mid2::kanMX6 rlc1-mCherry:natMX6 sid4-mCherry:hphMX6 ade6-M210 ura4-D18 leu1-32*	This study
Figure S2		

AP5501	*spn1-GFP:kanMX6 rlc1-mCherry:natMX6 sid4-mCherry:hphMX6 ade6-M210 ura4-D18 leu1-32*	This study
AP5515	*spn1-GFP:kanMX6 rlc1-mCherry:natMX6 sid4-mCherry:hphMX6 nda3-KM311 ade6-M210 ura4-D18 leu1-32*	This study
AP5678	*mid2-ENVY:kanMX6 rlc1-mCherry:natMX6 sid4-mCherry:hphMX6 ade6-M210 ura4-D18 leu1-32*	This study
AP5514	*mid2-ENVY:kanMX6 rlc1-mCherry:natMX6 sid4-mCherry:hphMX6 nda3-KM311 ade6-M210 ura4-D18 leu1-32*	This study
Figure S3		
AP6274	*mid2-13xMyc:natMX6 nda3-KM311 ade6-M210 ura4-D18 leu1-32*	This study
AP6069	*leu1+:Pmid1-mid2-GFP mid2-13xMyc:natMX6 nda3-KM311 ade6-M210 ura4-D18 leu1-32*	This study
AP6073	*leu1+:Pmid1-mid2ΔPH-GFP mid2-13xMyc:natMX6 nda3-KM311 ade6-M210 ura4-D18 leu1-32*	This study
AP6074	*leu1+:Pmid2-PHmid2-GFP mid2-13Myc:natMX6 nda3-KM311 ade6-M210 ura4-D18 leu1-32*	This study
AP5823	*mid2-13xMyc:Nat ade6-M210 ura4-D18 leu1-32*	This study
AP6276	*spn1-GFP:KanMX6 mid2-13XMyc:natMX6 ura4-D18 leu1-32*	This study
AP6280	*spn1-GFP:KanMX6 mid2-13XMyc:natMX6 nda3-KM311 ura4-D18 leu1-32*	This study
Figure S4		
AP5678	*mid2-ENVY:kanMX6 rlc1-mCherry:natMX6 sid4-mCherry:hphMX6 ade6-M210 ura4-D18 leu1-32*	This study
AP6271	*mid2-ENVY:kanMX6 rlc1-mCherry:natMX6 sid4-mCherry:hphMX6 cut7-24 ade6-M210 ura4-D18 leu1-32*	This study
Figure S5		
AP5501	*spn1-GFP:kanMX6 rlc1-mCherry:natMX6 sid4-mCherry:hphMX6 ade6-M210 ura4-D18 leu1-32*	This study
AP6313	*spn1-msfGFPΔN12:kanMX6 rlc1-mCherry:natMX6 sid4-mCherry:hphMX6 ade6-M210 ura4-D18 leu1-32*	This study
AP6334	*spn1-msfGFPΔN12:kanMX6 mid2::hphMX6 rlc1-mCherry:natMX6 sid4-mCherry:hphMX6 ade6-M210 ura4-D18 leu1-32*	This study

AP6324	*spn1-msfGFPΔN12:kanMX6 nda3-KM311 rlc1-mCherry:natMX6 sid4-mCherry:hphMX6 ade6-M210 ura4-D18 leu1-32*	This study
AP6234	*spn4ΔC6-msfGFPΔN7:kanMX6 rlc1-mCherry:natMX6 sid4-mCherry:hphMX6 ade6-M210 ura4-D18 leu1-32*	This study
Figure S6		
AP5678	*mid2-ENVY:kanMX6 rlc1-mCherry:natMX6 sid4-mCherry:hphMX6 ade6-M210 ura4-D18 leu1-32*	This study
AP5564	*mid2-ENVY:kanMX6 rlc1-mCherry:natMX6 sid4-mCherry:hphMX6 sid2-250 ade6-M210 ura4-D18 leu1-32*	This study
Figure S7		
AP5678	*mid2-ENVY:kanMX6 rlc1-mCherry:natMX6 sid4-mCherry:hphMX6 ade6-M210 ura4-D18 leu1-32*	This study
AP5855	*mid2-ENVY:kanMX6 rlc1-mCherry:natMX6 sid4-mCherry:hphMX6 cps1-191ade6-M210 ura4-D18 leu1-32*	This study

SUPPLEMENTAL FIGURE LEGENDS

Figure S1: In the absence of Mid2, septin localization is altered, but no effects on acto-myosin ring constriction are detected

A: Kymographs of the lateral region of the medial cortex (indicated in the scheme) of wild type (left) or *mid2Δ* cells (right) expressing Spn1-GFP, Rlc1-mCherry and Sid4-mCherry. Frames are spaced by 1 min intervals. The major transitions in the behavior of Spn1 from mitosis onset and the defects observed in absence of Mid2 are highlighted in bigger panels at the far right and indicated with a color-coded star. **B:** Plot showing total ring constriction duration in wild type and *mid2Δ* cells expressing Spn1-GFP, Rlc1-mCherry and Sid4-mCherry. Mean ± sd are shown. n=52 cells.

Figure S2: Under high CDK activity, septins appear as a broad band separated by the acto-myosin ring

A: Quantification of Spn1-GFP and Mid2-ENVY width over time in wild type (light green for Spn1-GFP and dark green for Mid2-ENVY) and *nda3-KM311* mutant cells (red for Spn1-GFP and dark red for Mid2-ENVY) incubated at 18°C during 8 hours. The last data point has been taken after switching the cells to 25°C for 1 hour. The average curves ± sd are displayed. n>500 cells. Fluorescence intensity analysis of Spn1-GFP, Rlc1-mcherry and Sid4-mcherry signal measured along the entire cell in epifluorescence images of the *nda3-KM311* cold sensitive mutant in a representative cell where the SPBs are aligned (**B**) or not (**C**) with respect to the ring position.

Figure S3: Mid2 is able to self-associate and to bind septins in the presence of high CDK activity

A: Co-immunoprecipitation assay between Mid2-13XMyc and full length Mid2-GFP, Mid2ΔPH-GFP or the PH domain of Mid2 tagged with GFP in *nda3-KM311* cells incubated at 18°C for 8 hours. Black asterisks show immunoglobulin bands; red asterisks show the expected Mid2 bands. Additional bands may represent degradation products of Mid2.**B:** Co-immunoprecipitation assay between Mid2-13XMyc and Spn1-GFP in control and *nda3-KM311* cells incubated at 18°C for 7 hours (lanes 5, 6, 7 and 8) and released for 1 hour at 25°C (lanes 1, 2, 3 and 4). Black asterisks show immunoglobulin bands; red asterisks show the expected Mid2 bands. Additional bands may represent degradation products of Mid2.

Figure S4: Mid2 appears as a broad band at the cell middle under high CDK activity. Time lapse imaging of wild type (**A**) or *cut7-24* cells (**C**) expressing Mid2-ENVY, Rlc1-mcherry and Sid4-mcherry incubated at 36°C. Maximum intensity projections of confocal images are shown. Time 0 corresponds to mitotic entry. Scale bars: 2 μm. Plot displaying Mid2-ENVY dynamics throughout cell division in control (**B**) and *cut7-24* cells (**D**). Mean ± sd are shown. n=45 cells in each strain. **E:** Quantification of the extent of Mid2-ENVY width compaction over time in wild type (dark green) and *cut7-24* cells (red). n=20 cells.

Figure S5: Localization and orientation measurements in Spn1-GFP and Spn4-conGFP wild type cells

A: Polar-plot histograms of GFP dipole orientations of Spn1-GFP filaments from wild type cells at different stages of cytokinesis (top panels). The number of analyzed cells per stage is indicated below each polar-plot histogram. Confocal images of Spn1-GFP from selected wild type cells (grayscale images) and an overlaid color-coded stick representation of the measured orientations (angles ρ) per analyzed pixel at each cytokinetic stage (bottom panels). The mean orientation of GFP dipoles per pixel is represented as a stick whose orientation and color are the measured angle ρ. Scale bar: 1 μm. **B**: Maximum intensity projection images of Spn1-GFP, Rlc1-mCherry and Sid4-mCherry in wild type cells (left) and Spn1-conGFP, Rlc1-mCherry and Sid4-mCherry (right) in wild type, *mid2Δ* and *nda3-KM311* cells at each stage of cytokinesis. Representative large field-of-view maximum intensity projection images of wild type *rlc1-mCherry sid4-mCherry* cells expressing Spn1-conGFP (**C**) or Spn4-conGFP (**D**) used for binning cells in each cytokinetic stage before polarimetry measurements. White asterisks in the insets in (D) point to septin rings in selected cells (dashed outlined rectangles), while white arrows point to ectopic cytoplasmic bar-like structures upon Spn4-conGFP expression. Scale bars: 10 μm. An example of a polar plot of dipole orientations in a Spn4-conGFP bar-like structure is shown on the right. A confocal image of the bar-like structure and an overlaid color-coded stick representation of the measured orientations in this structure are shown below the polar-plot histogram.

Scale bar: 1 µm. **E:** Examples of cells with Spn4-conGFP in septin rings during CR constriction (left) and early stages post constriction (right). Confocal images of selected cells (grayscale images) are shown together with the respective overlaid color-coded stick representation of the measured orientations and the polar-plot histograms.

Figure S6: Mid2 is poorly recruited to the division site under low SIN activity

Time lapse imaging of wild type (**A**) and *sid2-250* cells (**C**) expressing Mid2-ENVY, Rlc1-mCherry and Sid4-mCherry incubated at 36°C. Maximum intensity projections of confocal images are shown. Time 0 corresponds to mitotic entry. Scale bars: 2 µm. Plot showing Mid2-ENVY transitions throughout cell division in control (**B**) or *sid2-250* cells (**D**). Mean ± sd are shown. Wild type n=57 cells; *sid2-250* n=70 cells. **E:** Analysis of Mid2-ENVY intensity from mitotic onset throughout cell division in control (dark green) and *sid2-250* cells (dark red). The average curves ± sd are displayed. n=6 cells.

Figure S7: Mid2 recruitment to the division region is compromised in the Bgs1 mutant *cps1-191*.

Time lapse imaging of wild type (**A**) and *cps1-191* cells (**C**), expressing Mid2-ENVY, Rlc1-mCherry and Sid4-mCherry incubated at 36°C. Maximum intensity projections of confocal images are shown. Time 0 corresponds to mitotic entry. Scale bars: 2 µm. Plot showing Spn1-GFP transitions throughout cell division in wild type (**B**) or *cps1-191* cells (**D**). Mean ± sd are shown. Wild type n=50 cells *cps1-191* n=70 cells. **E:** Analysis of Mid2-ENVY intensity from mitotic onset throughout cell division in control (dark green) and *cps1-191* cells (dark red). The average curves ± sd are displayed. n=6 cells.

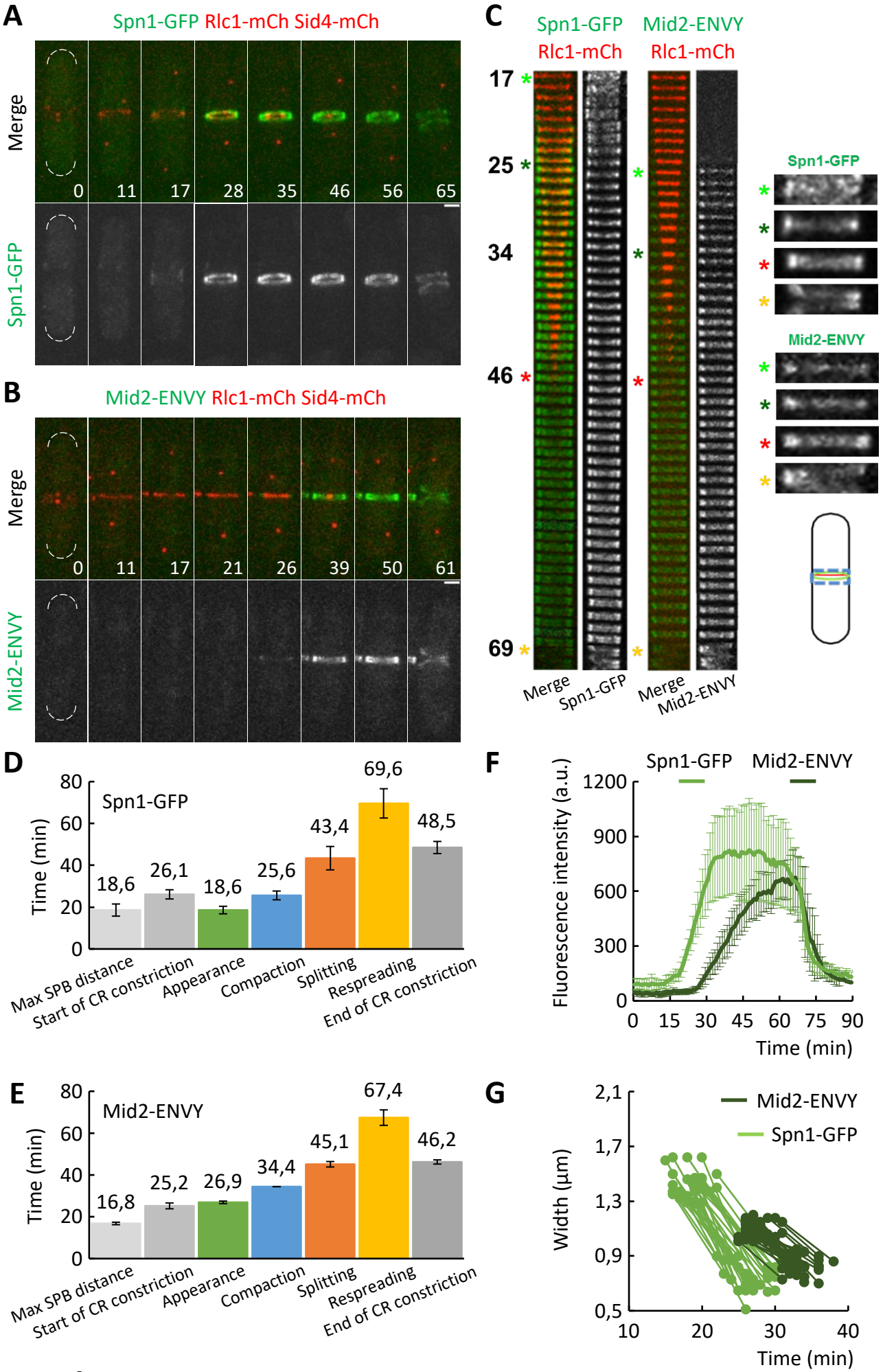
A
Spn1-GFP Rlc1-mCh Sid4-mCh
Merge
Spn1-GFP
0
11
17
28
35
46
56
65
B
Mid2-ENVY Rlc1-mCh Sid4-mCh
Merge
Mid2-ENVY
0
11
17
21
26
39
50
61
C
Spn1-GFP
Rlc1-mCh
Mid2-ENVY
Rlc1-mCh
17
25
34
46
69
Merge
Spn1-GFP
Merge
Mid2-ENVY
Spn1-GFP
Mid2-ENVY
D
Spn1-GFP
Time (min)
18,6
26,1
18,6
25,6
43,4
69,6
48,5
Max SPB distance
Start of CR constriction
Appearance
Compaction
Splitting
Respreading
End of CR constriction
E
Mid2-ENVY
Time (min)
16,8
25,2
26,9
34,4
45,1
67,4
46,2
Max SPB distance
Start of CR constriction
Appearance
Compaction
Splitting
Respreading
End of CR constriction
F
Spn1-GFP
Mid2-ENVY
Fluorescence intensity (a.u.)
Time (min)
G
Mid2-ENVY
Spn1-GFP
Width (µm)
Time (min)

Figure 1

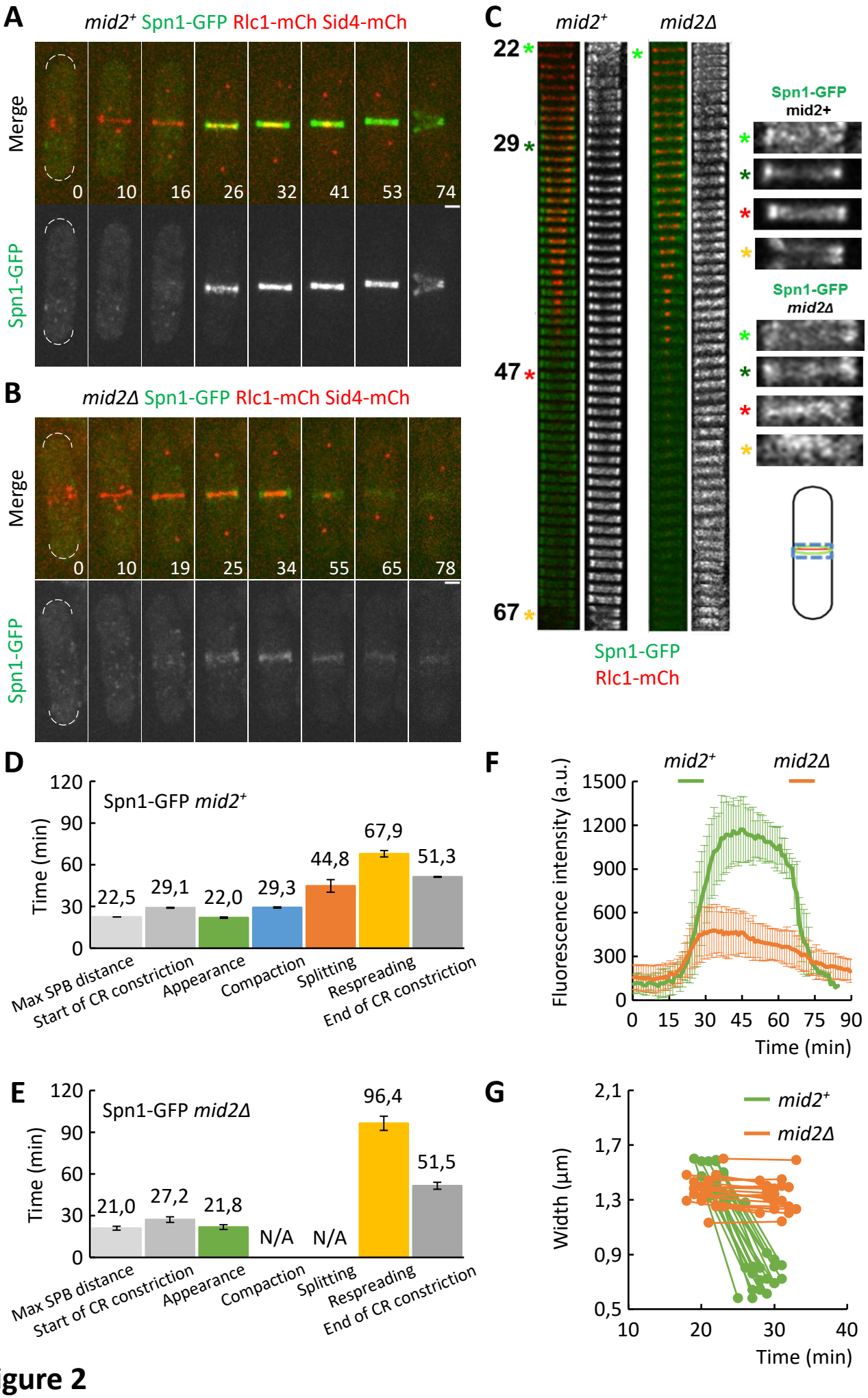
A
mid2⁺ Spn1-GFP Rlc1-mCh Sid4-mCh
Merge
Spn1-GFP
0
10
16
26
32
41
53
74
B
mid2Δ Spn1-GFP Rlc1-mCh Sid4-mCh
Merge
Spn1-GFP
0
10
19
25
34
55
65
78
C
mid2⁺
mid2Δ
22
29
47
67
Spn1-GFP
mid2+
Spn1-GFP
mid2Δ
Spn1-GFP
Rlc1-mCh
D
Spn1-GFP mid2⁺
Time (min)
120
90
60
30
0
22,5
29,1
22,0
29,3
44,8
67,9
51,3
Max SPB distance
Start of CR constriction
Appearance
Compaction
Splitting
Respreading
End of CR constriction
E
Spn1-GFP mid2Δ
Time (min)
120
90
60
30
0
21,0
27,2
21,8
N/A
N/A
96,4
51,5
Max SPB distance
Start of CR constriction
Appearance
Compaction
Splitting
Respreading
End of CR constriction
F
mid2⁺
mid2Δ
Fluorescence intensity (a.u.)
1500
1200
900
600
300
0
0
15
30
45
60
75
90
Time (min)
G
mid2⁺
mid2Δ
Width (µm)
2,1
1,7
1,3
0,9
0,5
10
20
30
40
Time (min)

Figure 2

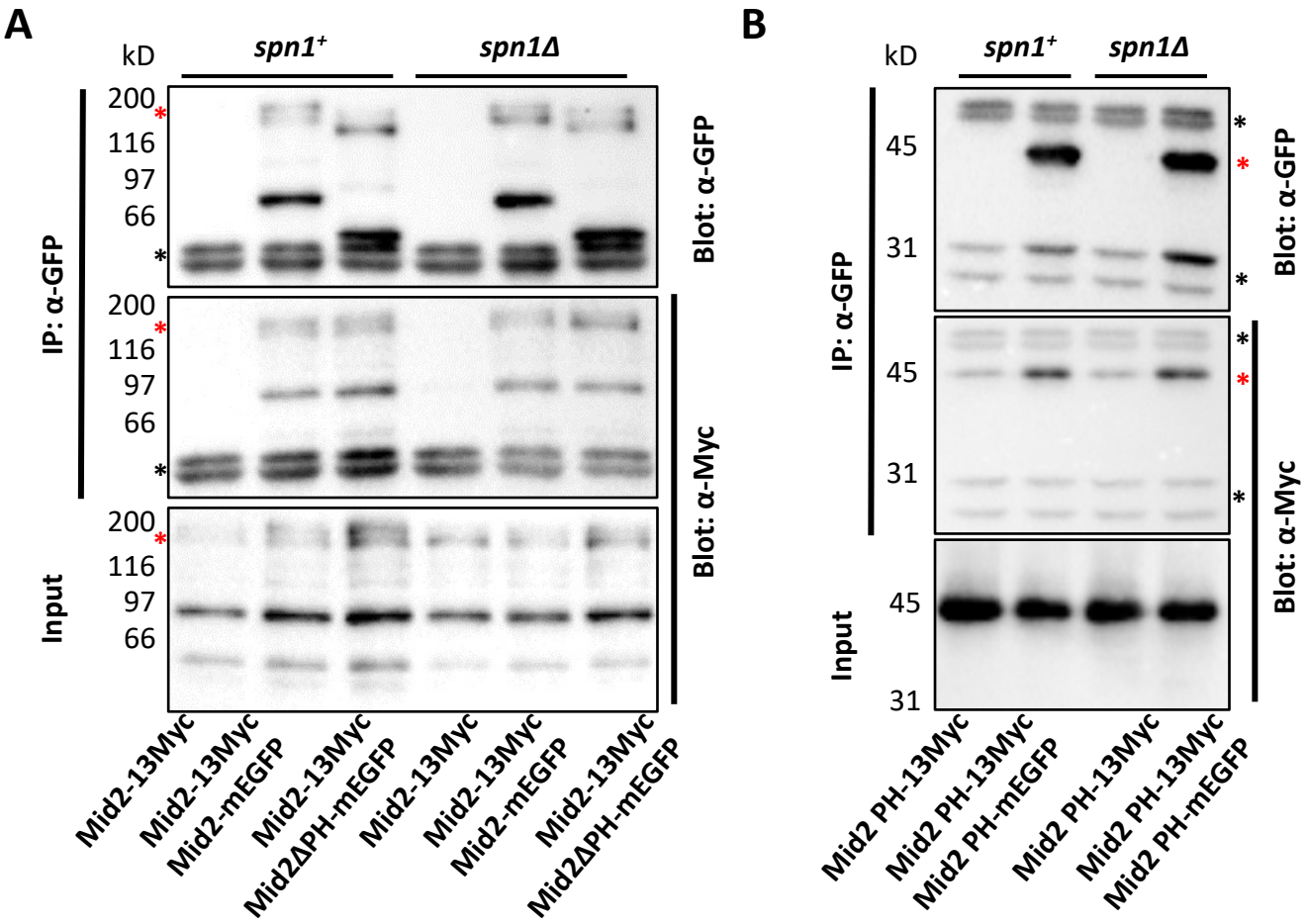
A
kD
spn1+
spn1Δ
200
116
97
66
IP: α-GFP
Input
Blot: α-GFP
Blot: α-Myc
Mid2-13Myc
Mid2-mEGFP
Mid2ΔPH-mEGFP
B
45
31
Mid2 PH-13Myc
Mid2 PH-mEGFP

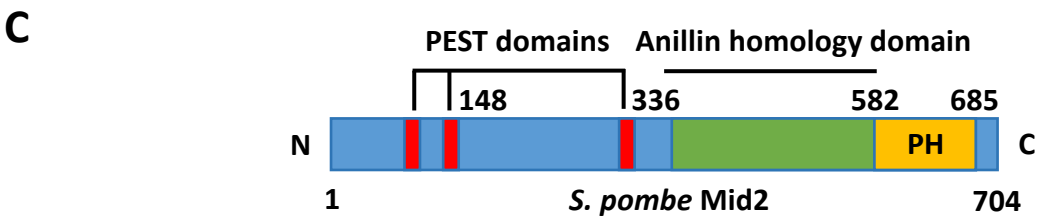
C
PEST domains
Anillin homology domain
148
336
582
685
N
C
PH
1
S. pombe Mid2
704

Figure 3

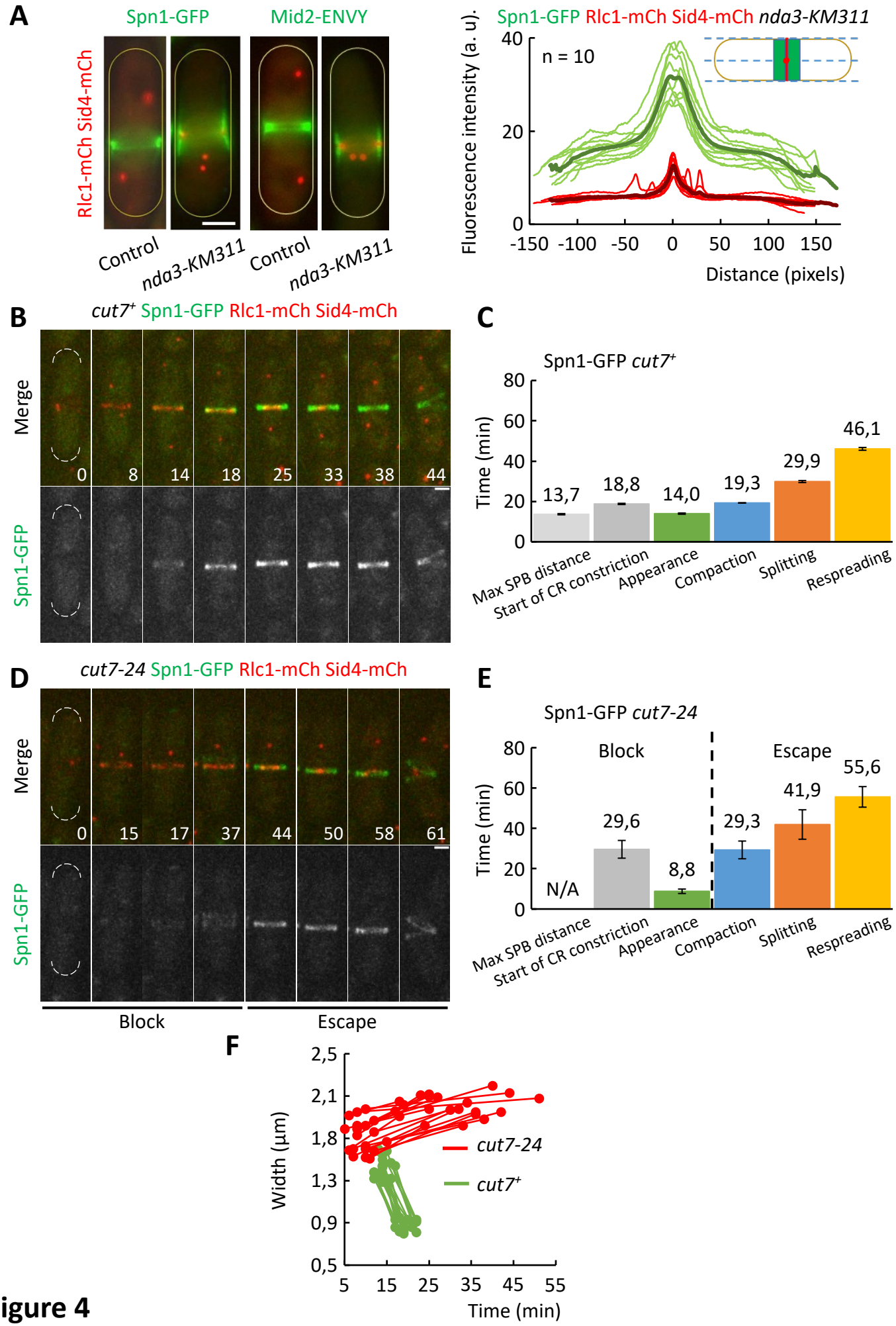
A
Spn1-GFP
Mid2-ENVY
Rlc1-mCh Sid4-mCh
Control
nda3-KM311
Control
nda3-KM311
Spn1-GFP Rlc1-mCh Sid4-mCh nda3-KM311
n = 10
Fluorescence intensity (a. u.)
Distance (pixels)
B
cut7+ Spn1-GFP Rlc1-mCh Sid4-mCh
Merge
Spn1-GFP
C
Spn1-GFP cut7+
Time (min)
13,7
18,8
14,0
19,3
29,9
46,1
Max SPB distance
Start of CR constriction
Appearance
Compaction
Splitting
Respreading
D
cut7-24 Spn1-GFP Rlc1-mCh Sid4-mCh
Block
Escape
E
Spn1-GFP cut7-24
N/A
29,6
8,8
29,3
41,9
55,6
F
Width (µm)
cut7-24
cut7+
Time (min)

Figure 4

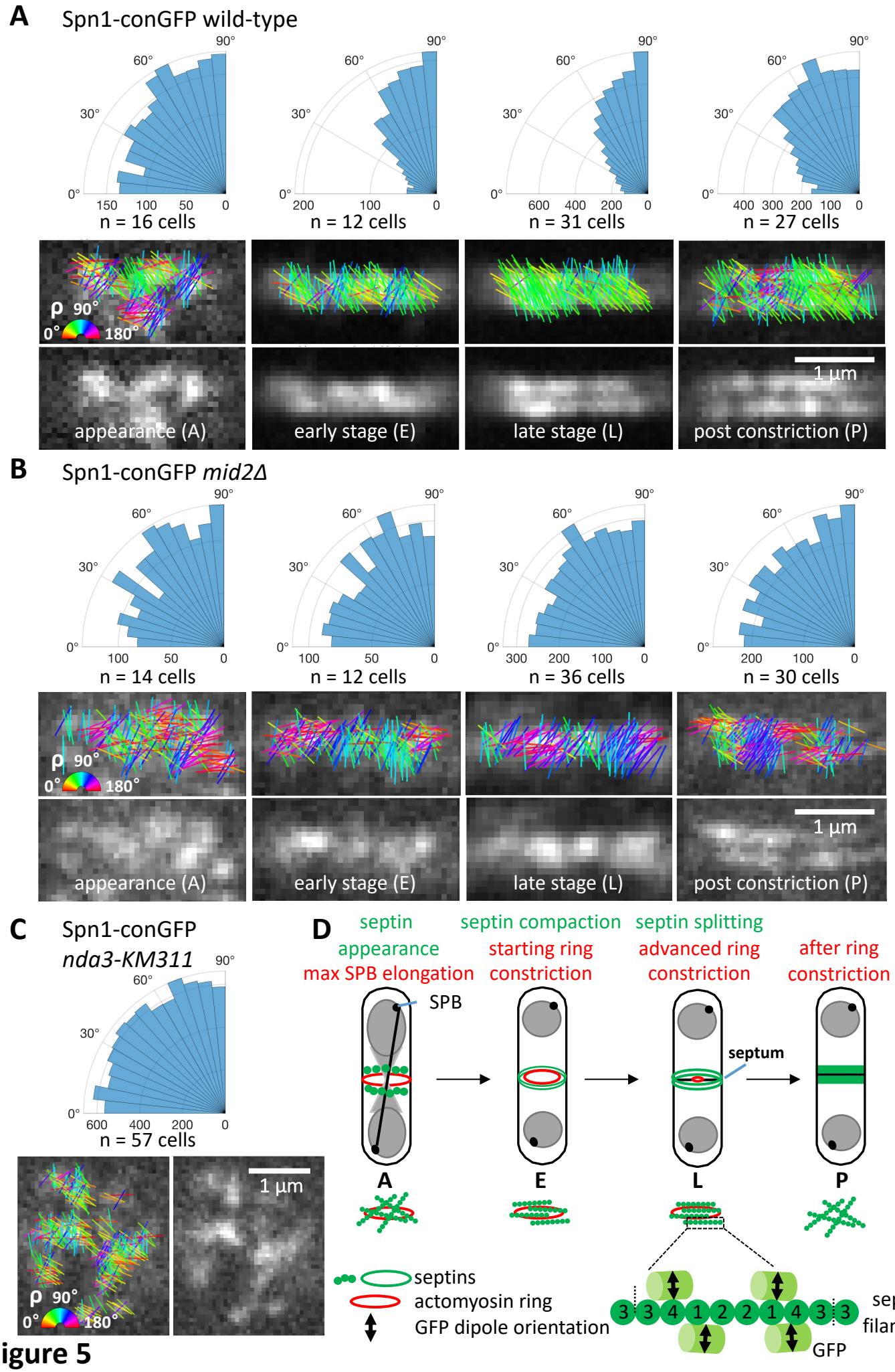
A
Spn1-conGFP wild-type
n = 16 cells
n = 12 cells
n = 31 cells
n = 27 cells
ρ 90°
0° 180°
1 µm
appearance (A)
early stage (E)
late stage (L)
post constriction (P)
B
Spn1-conGFP mid2Δ
n = 14 cells
n = 12 cells
n = 36 cells
n = 30 cells
C
Spn1-conGFP
nda3-KM311
n = 57 cells
D
septin appearance
max SPB elongation
septin compaction
starting ring constriction
septin splitting
advanced ring constriction
after ring constriction
SPB
septum
A
E
L
P
septins
actomyosin ring
GFP dipole orientation
septin filament
GFP

Figure 5

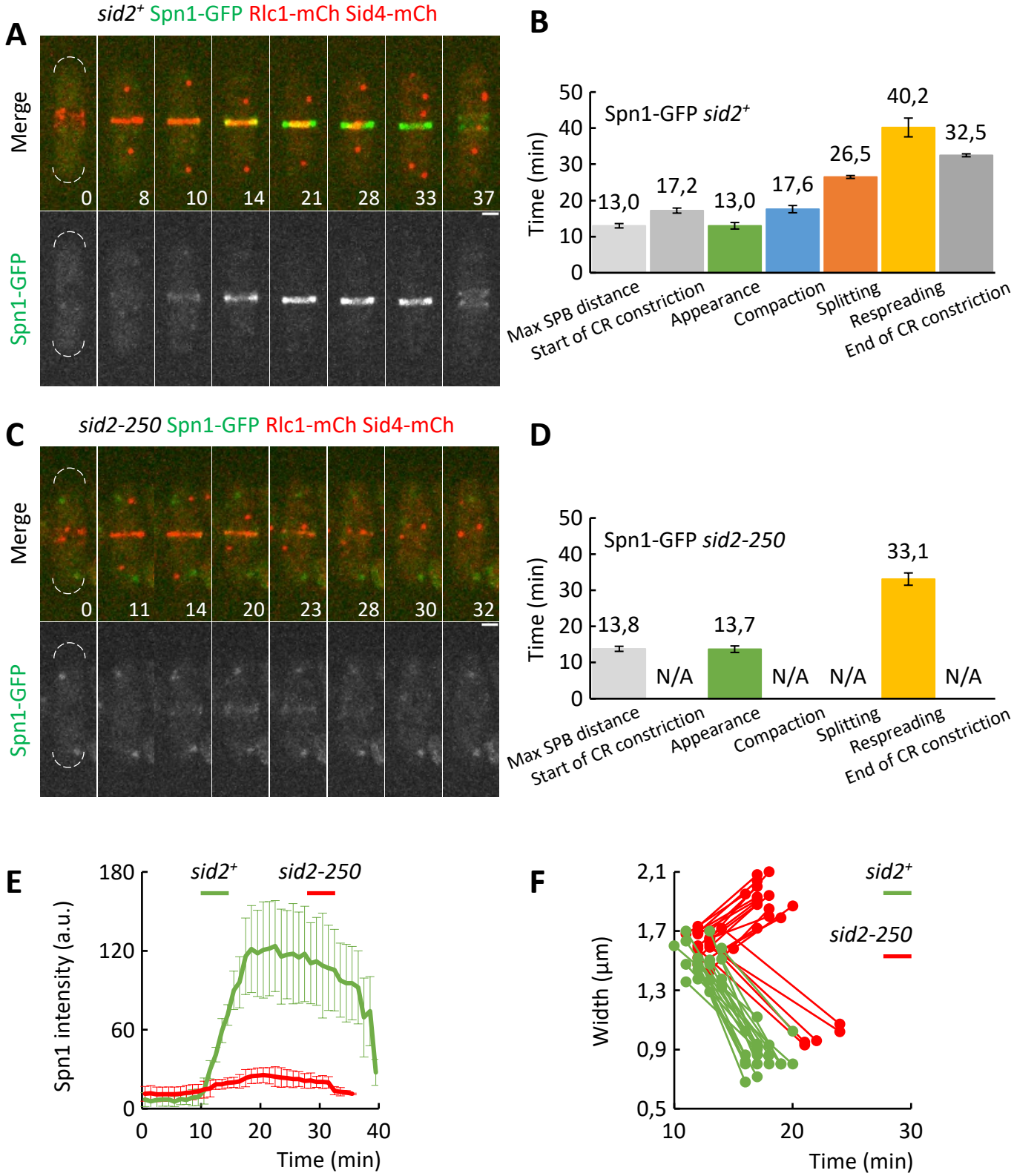
A
sid2+ Spn1-GFP Rlc1-mCh Sid4-mCh
Merge
Spn1-GFP
0
8
10
14
21
28
33
37
B
Spn1-GFP sid2+
Time (min)
13,0
17,2
13,0
17,6
26,5
40,2
32,5
Max SPB distance
Start of CR constriction
Appearance
Compaction
Splitting
Respreading
End of CR constriction
C
sid2-250 Spn1-GFP Rlc1-mCh Sid4-mCh
Merge
Spn1-GFP
0
11
14
20
23
28
30
32
D
Spn1-GFP sid2-250
Time (min)
13,8
N/A
13,7
N/A
N/A
33,1
N/A
Max SPB distance
Start of CR constriction
Appearance
Compaction
Splitting
Respreading
End of CR constriction
E
sid2+
sid2-250
Spn1 intensity (a.u.)
Time (min)
F
sid2+
sid2-250
Width (µm)
Time (min)

Figure 6

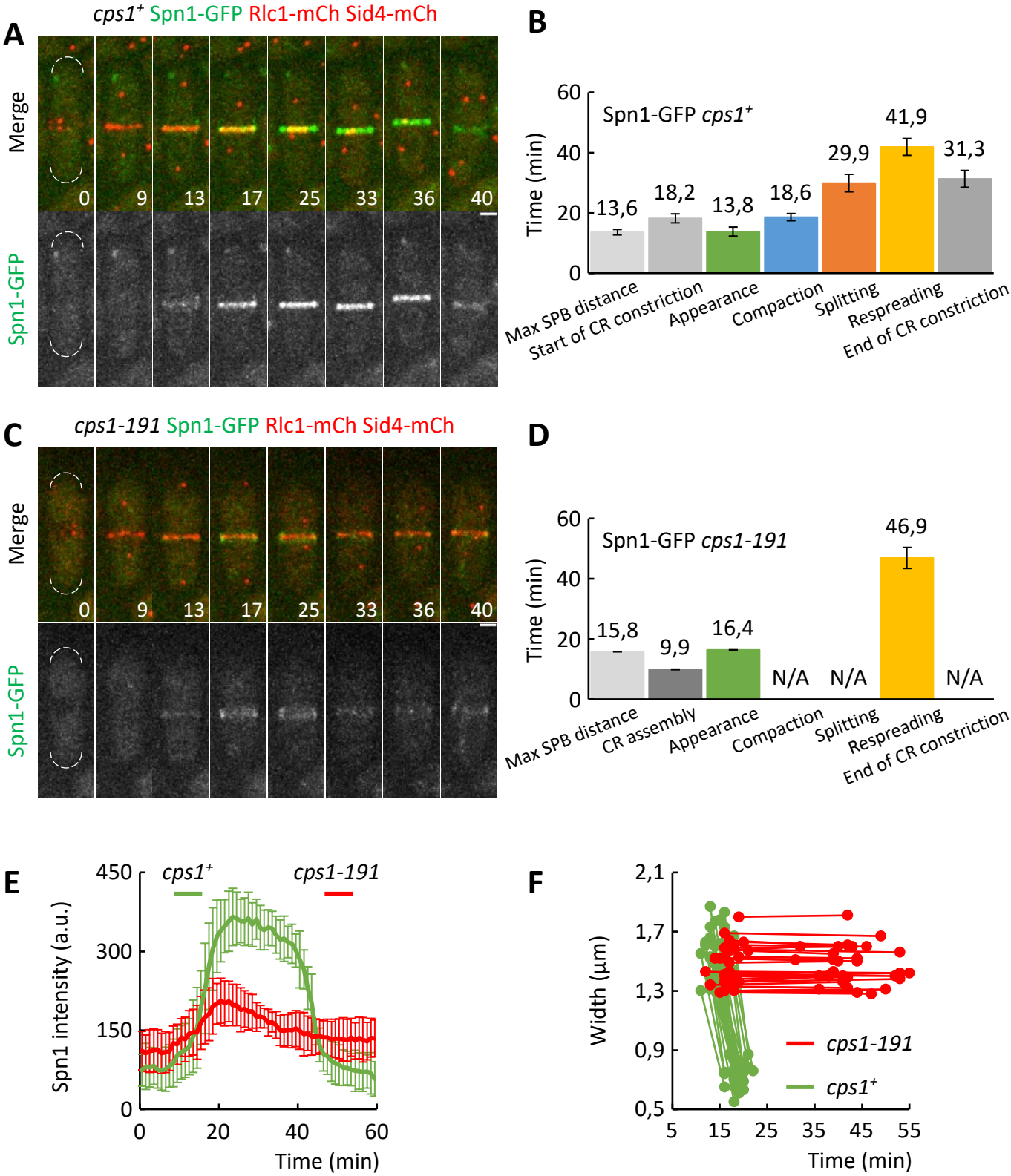
A
cps1+ Spn1-GFP Rlc1-mCh Sid4-mCh
Merge
Spn1-GFP
0
9
13
17
25
33
36
40
B
Spn1-GFP cps1+
Time (min)
60
40
20
0
13,6
18,2
13,8
18,6
29,9
41,9
31,3
Max SPB distance
Start of CR constriction
Appearance
Compaction
Splitting
Respreading
End of CR constriction
C
cps1-191 Spn1-GFP Rlc1-mCh Sid4-mCh
Merge
Spn1-GFP
0
9
13
17
25
33
36
40
D
Spn1-GFP cps1-191
Time (min)
60
40
20
0
15,8
9,9
16,4
N/A
N/A
46,9
N/A
Max SPB distance
CR assembly
Appearance
Compaction
Splitting
Respreading
End of CR constriction
E
Spn1 intensity (a.u.)
450
300
150
0
cps1+
cps1-191
0
20
40
60
Time (min)
F
Width (µm)
2,1
1,7
1,3
0,9
0,5
cps1-191
cps1+
5
15
25
35
45
55
Time (min)

Figure 7

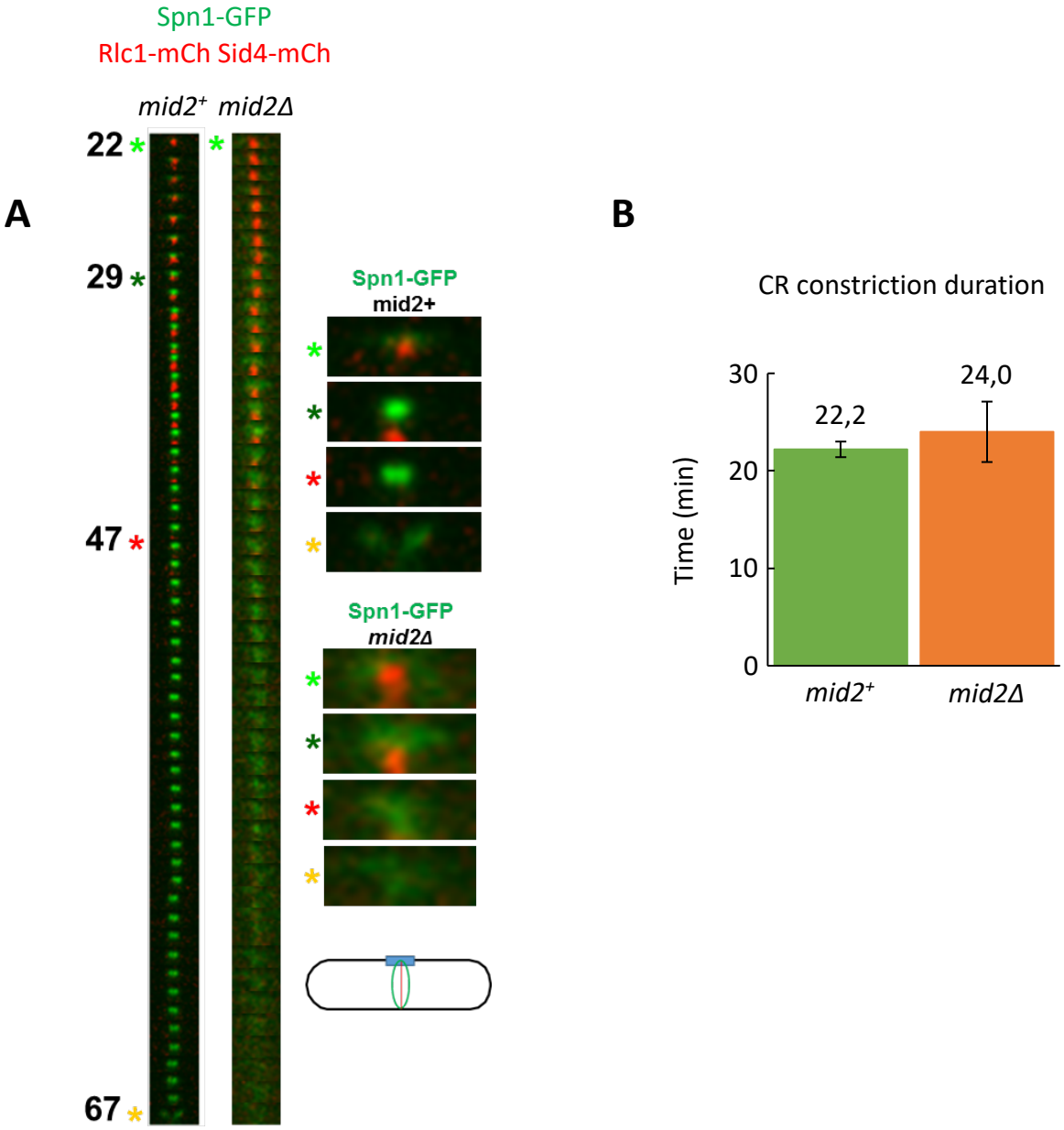
Spn1-GFP
Rlc1-mCh Sid4-mCh
mid2⁺ mid2Δ
A
22
29
47
67
Spn1-GFP
mid2+
Spn1-GFP
mid2Δ
B
CR constriction duration
Time (min)
30
20
10
0
22,2
24,0
mid2⁺
mid2Δ

Figure S1

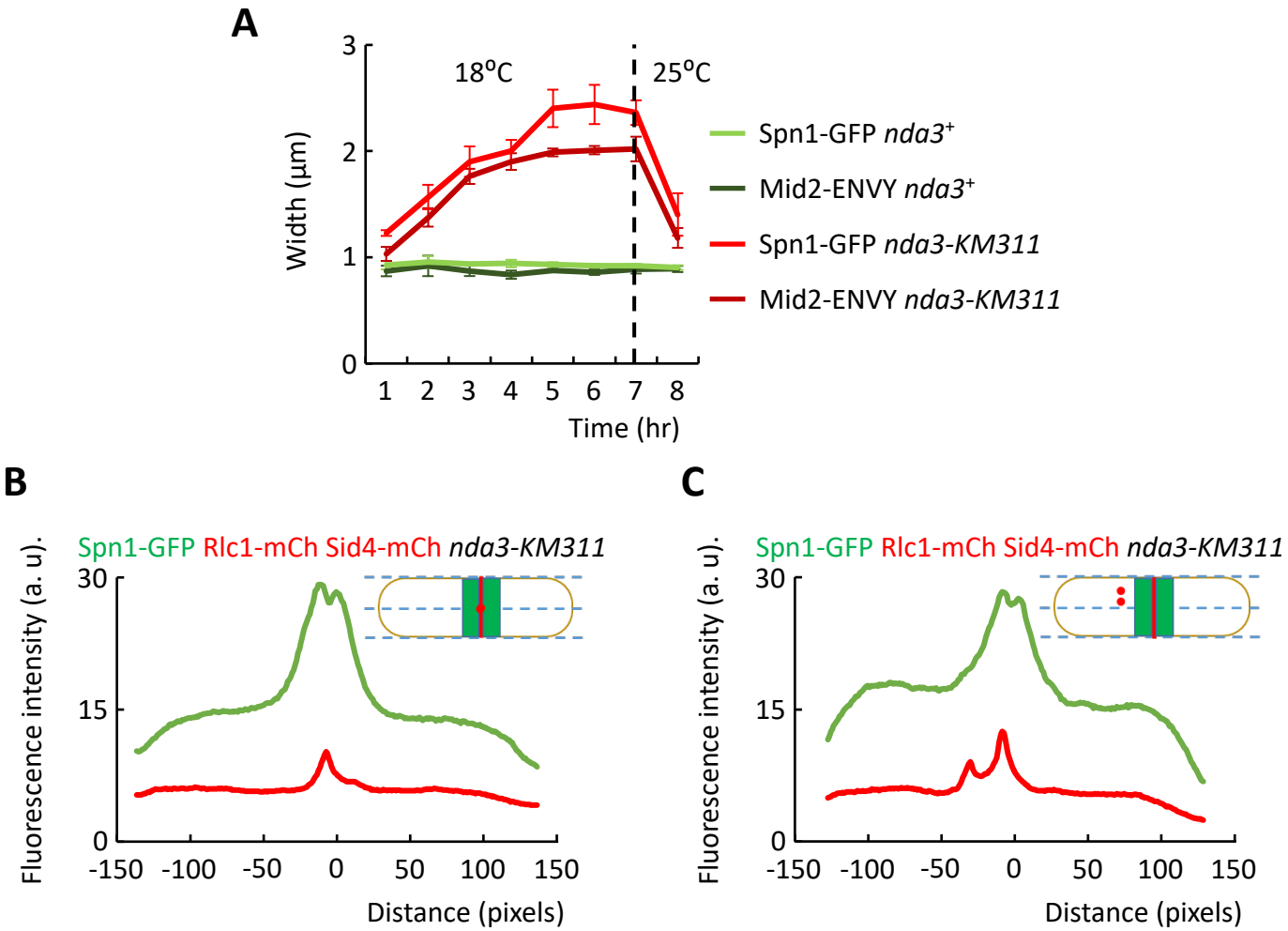
A
18°C
25°C
Width (µm)
Time (hr)
Spn1-GFP nda3+
Mid2-ENVY nda3+
Spn1-GFP nda3-KM311
Mid2-ENVY nda3-KM311
B
Spn1-GFP Rlc1-mCh Sid4-mCh nda3-KM311
Fluorescence intensity (a. u).
Distance (pixels)
C
Spn1-GFP Rlc1-mCh Sid4-mCh nda3-KM311
Fluorescence intensity (a. u).
Distance (pixels)

Figure S2

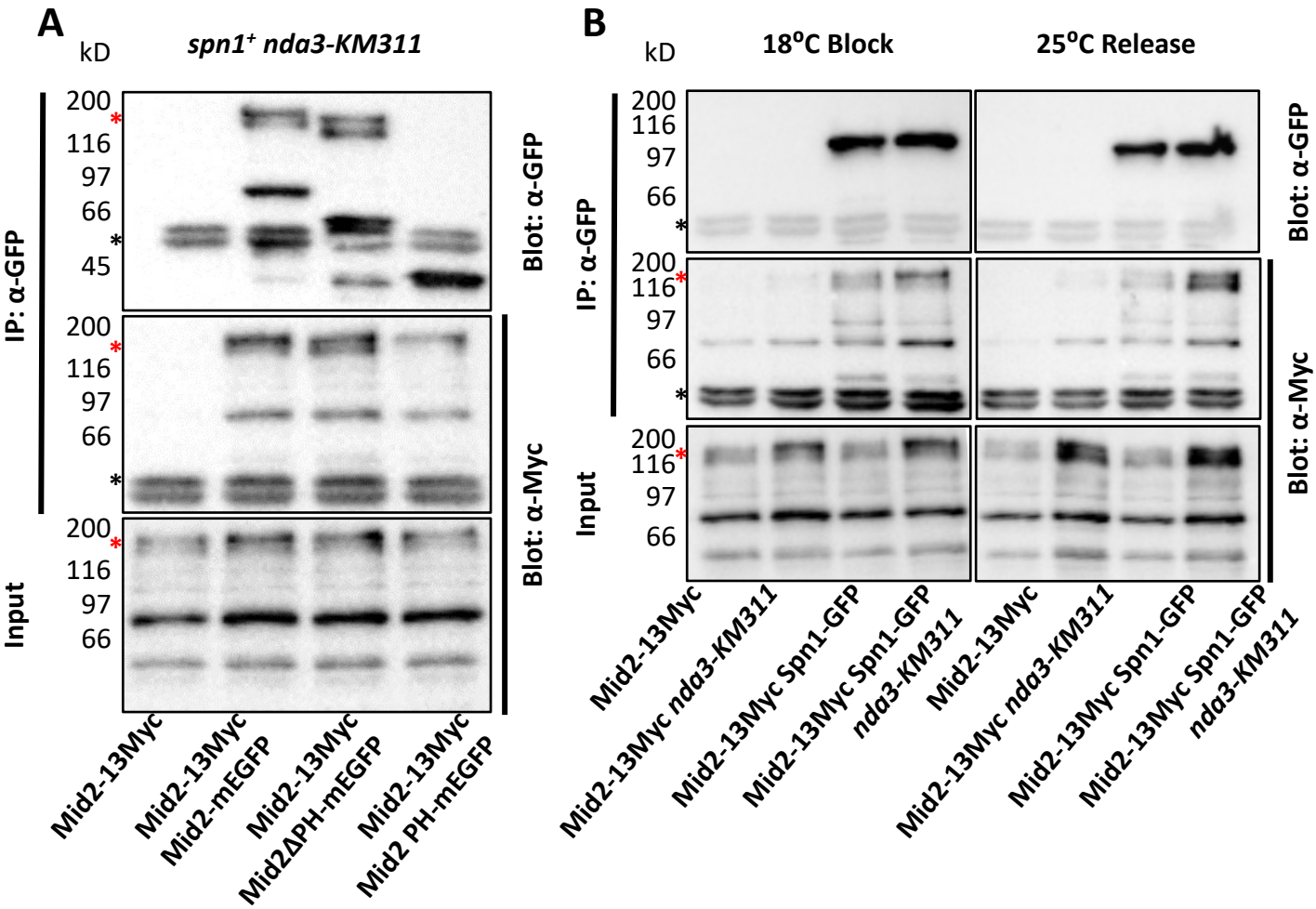
A
kD
spn1+ nda3-KM311
IP: α-GFP
Input
Blot: α-GFP
Blot: α-Myc
200
116
97
66
45
Mid2-13Myc
Mid2-13Myc Mid2-mEGFP
Mid2-13Myc Mid2ΔPH-mEGFP
Mid2-13Myc Mid2 PH-mEGFP
B
kD
18°C Block
25°C Release
IP: α-GFP
Input
Blot: α-GFP
Blot: α-Myc
Mid2-13Myc
Mid2-13Myc nda3-KM311
Mid2-13Myc Spn1-GFP
Mid2-13Myc Spn1-GFP nda3-KM311

Figure S3

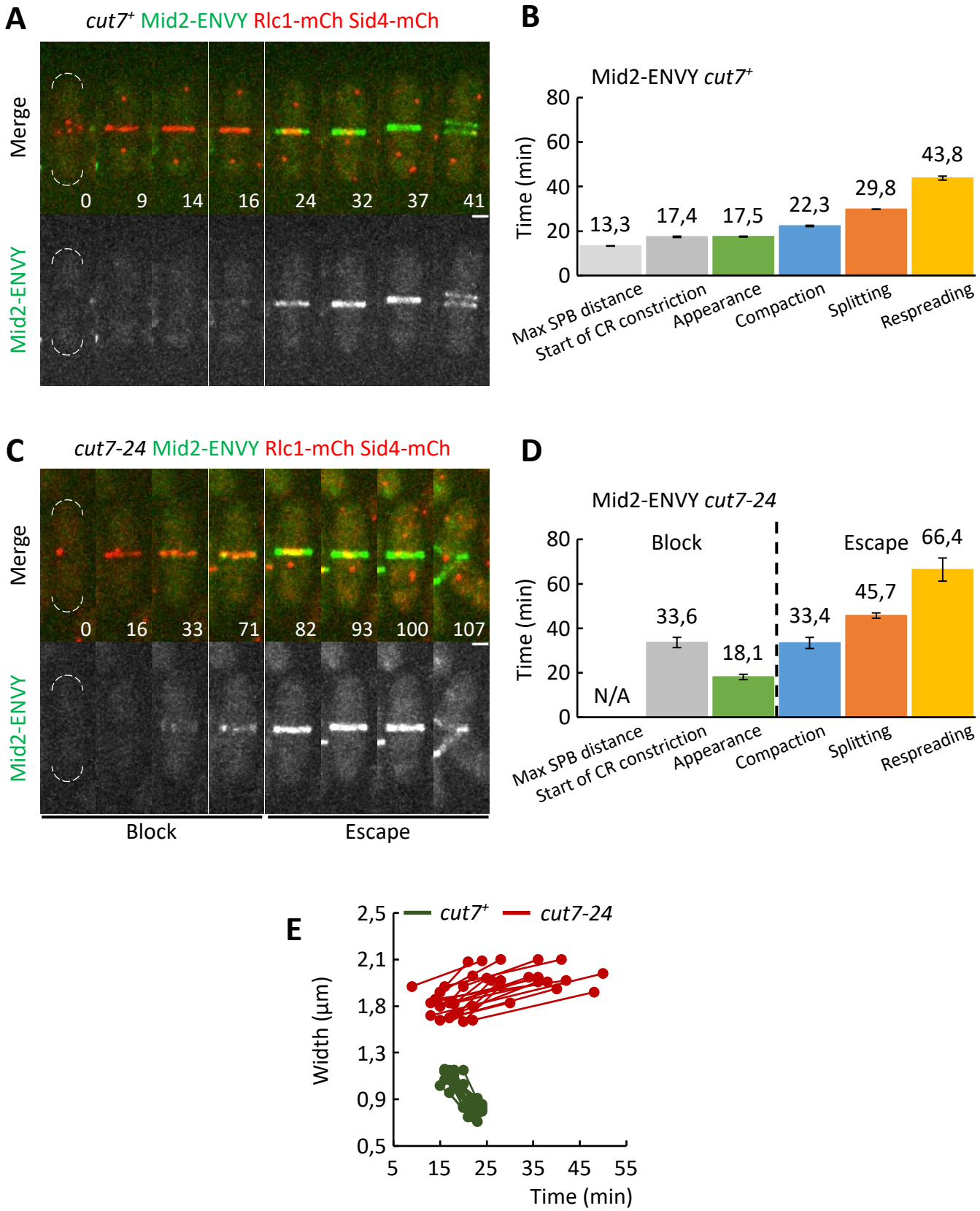
A
cut7+ Mid2-ENVY Rlc1-mCh Sid4-mCh
Merge
Mid2-ENVY
0
9
14
16
24
32
37
41
B
Mid2-ENVY cut7+
Time (min)
80
60
40
20
0
13,3
17,4
17,5
22,3
29,8
43,8
Max SPB distance
Start of CR constriction
Appearance
Compaction
Splitting
Respreading
C
cut7-24 Mid2-ENVY Rlc1-mCh Sid4-mCh
Merge
Mid2-ENVY
0
16
33
71
82
93
100
107
Block
Escape
D
Mid2-ENVY cut7-24
Time (min)
80
60
40
20
0
Block
Escape
N/A
33,6
18,1
33,4
45,7
66,4
Max SPB distance
Start of CR constriction
Appearance
Compaction
Splitting
Respreading
E
cut7+
cut7-24
Width (µm)
2,5
2,1
1,8
1,3
0,9
0,5
5
15
25
35
45
55
Time (min)

Figure S4

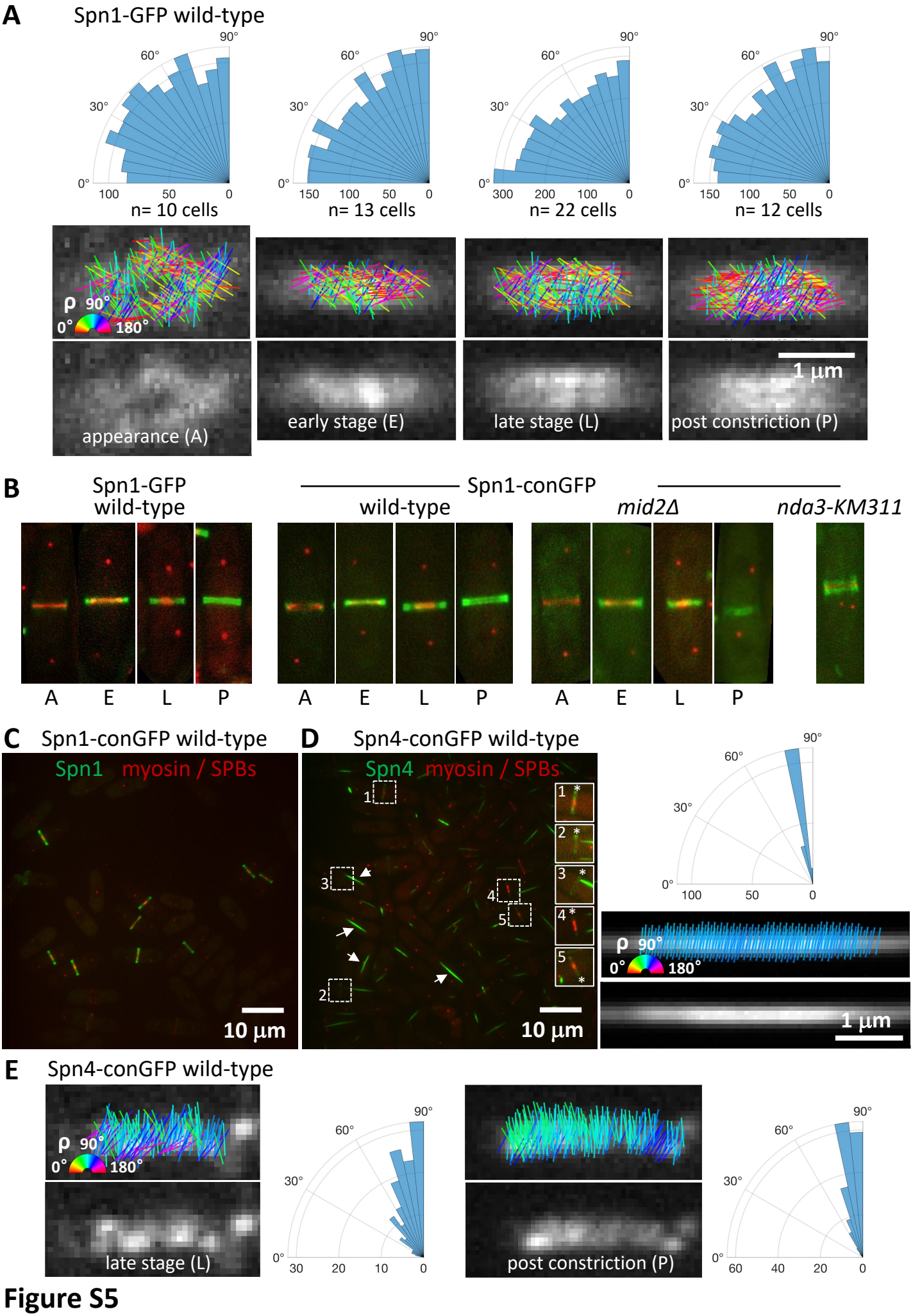
A
Spn1-GFP wild-type
n= 10 cells
n= 13 cells
n= 22 cells
n= 12 cells
ρ 90°
0° 180°
appearance (A)
early stage (E)
late stage (L)
post constriction (P)
1 µm
B
Spn1-GFP wild-type
Spn1-conGFP
wild-type
mid2Δ
nda3-KM311
A E L P
C
Spn1-conGFP wild-type
Spn1 myosin / SPBs
10 µm
D
Spn4-conGFP wild-type
Spn4 myosin / SPBs
10 µm
1 µm
E
Spn4-conGFP wild-type
late stage (L)
post constriction (P)

Figure S5

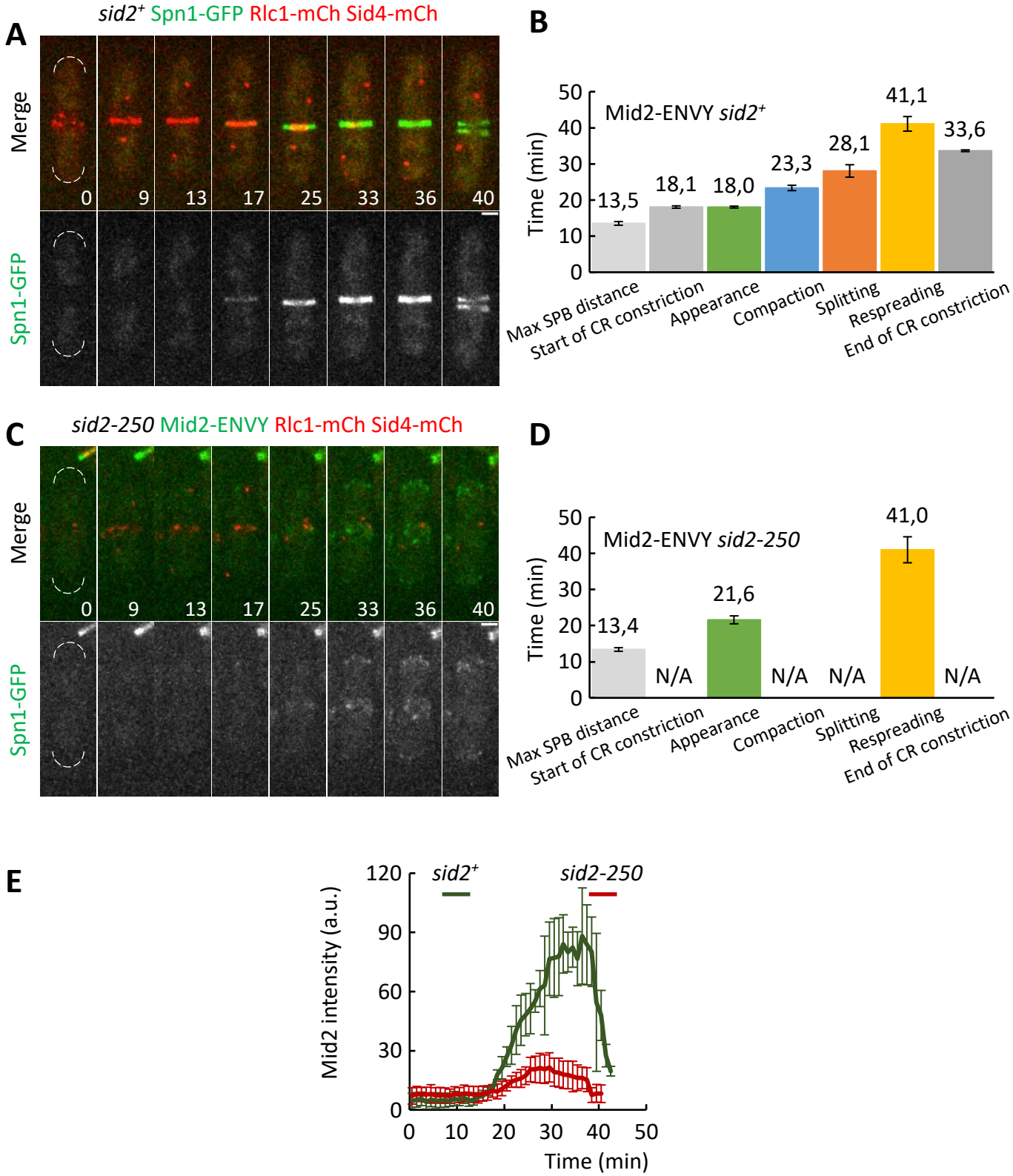
A
sid2+ Spn1-GFP Rlc1-mCh Sid4-mCh
Merge
Spn1-GFP
0
9
13
17
25
33
36
40
B
Mid2-ENVY sid2+
Time (min)
13,5
18,1
18,0
23,3
28,1
41,1
33,6
Max SPB distance
Start of CR constriction
Appearance
Compaction
Splitting
Respreading
End of CR constriction
C
sid2-250 Mid2-ENVY Rlc1-mCh Sid4-mCh
D
Mid2-ENVY sid2-250
13,4
N/A
21,6
N/A
N/A
41,0
N/A
E
sid2+
sid2-250
Mid2 intensity (a.u.)
Time (min)

Figure S6

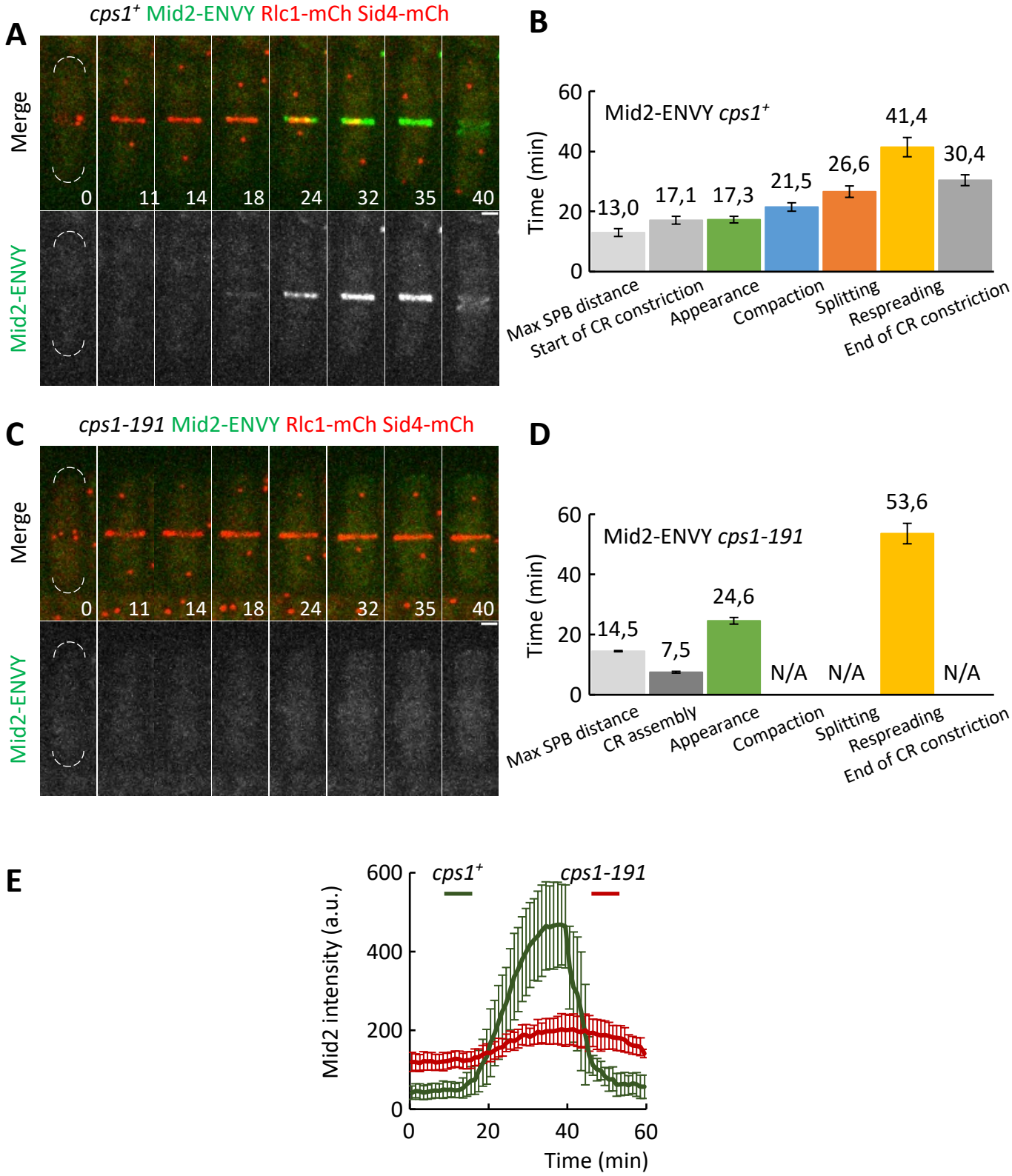
A
cps1+ Mid2-ENVY Rlc1-mCh Sid4-mCh
Merge
Mid2-ENVY
0
11
14
18
24
32
35
40
B
Mid2-ENVY cps1+
Time (min)
60
40
20
0
13,0
17,1
17,3
21,5
26,6
41,4
30,4
Max SPB distance
Start of CR constriction
Appearance
Compaction
Splitting
Respreading
End of CR constriction
C
cps1-191 Mid2-ENVY Rlc1-mCh Sid4-mCh
Merge
Mid2-ENVY
0
11
14
18
24
32
35
40
D
Mid2-ENVY cps1-191
Time (min)
60
40
20
0
14,5
7,5
24,6
N/A
N/A
53,6
N/A
Max SPB distance
CR assembly
Appearance
Compaction
Splitting
Respreading
End of CR constriction
E
cps1+
cps1-191
Mid2 intensity (a.u.)
600
400
200
0
0
20
40
60
Time (min)

Figure S7